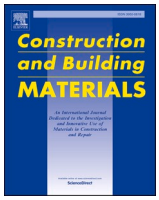
Construction and Building Materials 479 (2025) 141078



Contents lists available at ScienceDirect

Construction and Building Materials

journal homepage: www.elsevier.com/locate/conbuildmat



Influence of process parameters on the physical and material properties of WAAM steels

Athina Spinasa [a], Ben Weber [a], Xin Meng [a,*], Ruizhi Zhang [a], Masashi Nitawaki [b], Leroy Gardner [a]

[a] Department of Civil and Environmental Engineering, Imperial College London, South Kensington Campus, London SW7 2AZ, UK
[b] Shimizu Corporation, 2-16-1 Kyobashi, Chuo-ku , Tokyo 104-8370, Japan

ARTICLE INFO

Keywords:
X-ray Computed Tomography (XCT) scans
Mechanical properties
Microstructural analysis
Tensile coupons
Testing
Wire arc additive manufacturing (WAAM)

ABSTRACT

Wire arc additive manufacturing (WAAM) is a metal 3D printing technique that offers the opportunity to fabricate large-scale structural components with high geometric flexibility and reduced material waste. This study aims to investigate the influence of different process parameters and cooling methods on the physical, mechanical and microstructural properties of WAAM steels with a view to assessing their suitability for use in construction. Six WAAM steel plates with nominal thicknesses of 3.5 mm, 5 mm, 8 mm and 12 mm, printed using ER90S-D2 welding wire, different process parameters and active or passive cooling, were examined. A total of 72 tensile coupons extracted at different orientations relative to the print layers with either as-built or machined surface conditions were tested. 3D laser scanning was performed to capture the as-built surface undulations and facilitate the calculation of surface roughness. X-ray computed tomography (XCT) scanning was conducted on selected coupon specimens to examine the printing defects. The tensile testing revealed that the WAAM steels exhibited largely isotropic elastic behaviour, which aligned with the weak crystallographic texture found in the microstructural analysis. The as-built geometry led to notable reductions in strength and ductility, particularly in as-built specimens loaded perpendicularly to the print layers. The results also showed that the thicker WAAM plates generally exhibited lower yield strength due mainly to the slower cooling rate leading to coarser grains, as revealed by the microstructural examinations. High porosity was observed in the XCT scan results of some coupons and was shown to significantly reduce the material ductility. Finally, the adopted active cooling method was found to increase productivity, but to have a minimal effect on the resulting mechanical properties. The presented findings contribute to the understanding of the material behaviour of WAAM steel and its link to the key process parameters.

1. Introduction

Metal additive manufacturing (AM) has emerged as an innovative solution for a variety of industries for its ability to produce intricate geometries with enhanced automation and its potential to reduce material usage and wastage [1–4]. According to ISO/ASTM 52900 [5], metal additive manufacturing techniques include sheet lamination (SHL), powder bed fusion (PBF), and directed energy deposition (DED). One of the pre-eminent AM techniques, which falls under the umbrella of directed energy deposition (DED), is wire arc additive manufacturing (WAAM), which utilises an electric arc as the heat source and welding wire as feedstock to produce metal parts layer-by-layer. WAAM is deemed to be the most promising technique for the construction industry because of its utilisation of widely accessible welding technology and feedstock wire, and its capability to produce large and intricate components both quickly and economically [6–8]. A number of examples of practical applications of WAAM in construction have emerged. For instance, the MX3D bridge in Amsterdam [9] demonstrates the scale at which the technology can be used, the steel bridge in Darmstadt [10] showed the potential for on-site production, the optimised steel trusses [11], the Imperial-Shimizu footbridge [12] in London illustrated the potential for material savings, the WAAM canopy in Hong Kong [13] highlighted the elegance of form that can be achieved, while the connection nodes presented in [14,15] showed the ability to produce intricate details.

An important challenge for the more widespread adoption of WAAM

* Corresponding author.
E-mail address: xin.meng15@imperial.ac.uk (X. Meng).

https://doi.org/10.1016/j.conbuildmat.2025.141078
Received 17 December 2024; Received in revised form 11 March 2025; Accepted 26 March 2025
Available online 29 April 2025
0950-0618/© 2025 The Authors. Published by Elsevier Ltd. This is an open access article under the CC BY license (http://creativecommons.org/licenses/by/4.0/).

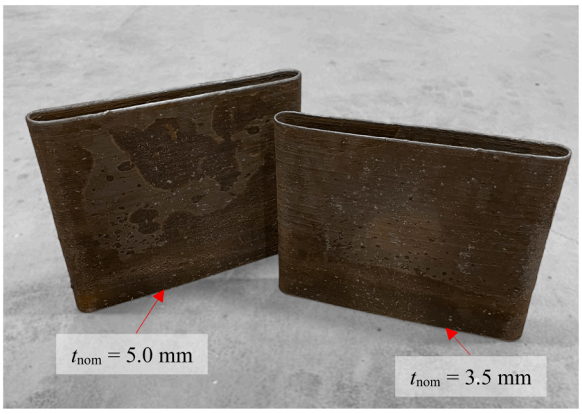


Fig. 1. Typical WAAM oval flat-sided tubes after removal from the base plate.

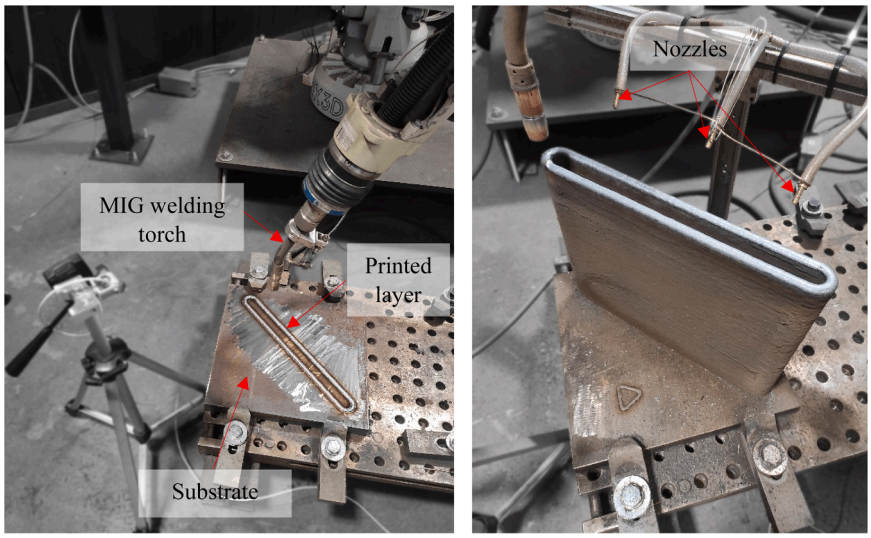


Fig. 2. (a) Overall WAAM setup and (b) application of active cooling for production of oval tubes.

Table 1
Mechanical properties of as-welded ER90S-D2 wire, as stated in the wire certificate.

Mechanical property	Minimum guaranteed value	Measured value
Yield strength f_y (MPa)	560	607
Ultimate strength f_u (MPa)	620	637
Elongation at fracture ε_f (%)	18	18
Charpy V-notch impact energy at −70°C A_v (J)	47	60

material in construction relates to the variability and uncertainty in the mechanical properties [4,16] as well as the presence of defects and the dependency on the printing conditions. An increasing number of studies have been conducted to explore the mechanical properties of WAAM materials, including carbon steels [17–24], stainless steels [25–31], titanium alloys [32,33], aluminium alloys [34–36] and others [37]. High strength steels, recognised for their high strength-to-weight ratio and the potential for lighter components, have been adopted across the aerospace, automotive and construction sectors [38–43]. Investigations into the material properties of WAAM high strength steels have also been carried out by [17,38,39,44–47]. However, knowledge gaps still exist, particularly regarding the effects of process parameters, such as arc current, travel speed, inter-layer cooling time and toolpath, which have been shown to considerably influence the microstructure and the mechanical properties of the printed material [48–51]. The lack of knowledge of the link between the process parameters and the resulting mechanical properties hinders the wider adoption of WAAM in

Table 2
Chemical composition of ER90S-D2 wire in (%), as stated in the wire certificate.

C	Si	Mn	S	Cu	Cr	Mo	Ni	Co	Fe
0.10	0.71	1.89	0.011	0.025	0.04	0.44	0.05	0.013	Balance

Table 3
Process parameters used for WAAM ovals.

	t_{nom} = 3.5 mm	t_{nom} = 5 mm	t_{nom} = 8 mm	t_{nom} = 12 mm
Wire grade	ER90S-D2	ER90S-D2	ER90S-D2	ER90S-D2
Wire diameter (mm)	1.2	1.2	1.2	1.2
Wire feed rate (m/min)	2.3	2.7	3.5	3.7
Average layer height (mm)	1.1	1.2	1.7	1.7
Interpass temperature (°C)	350	350	350	350
Stick out (mm)	9–12	9–12	9–12	9–12
Welding voltage (V)	14.6	15.6	16.8	20
Welding current (A)	102	117	152	129
Shield gas composition	98% Ar, 2% CO_2	98% Ar, 2% CO_2	98% Ar, 2% CO_2	98% Ar, 2% CO_2
Shield gas flow rate (L/min)	16.0	16.0	16.0	16.0
Cooling method	Passive	Passive	Active | passive	Active | passive
Toolpath	Single pass	Single pass	Double pass	Weaving

load-bearing applications.

Hence, the aim of this study is to explore the influence of varying process parameters on the resulting material properties of WAAM steels. A comprehensive experimental programme has been conducted on WAAM carbon steel printed using ER90S-D2 welding wire. The investigation encompassed four nominal wall thicknesses – 3.5 mm, 5 mm, 8 mm, and 12 mm, achieved with different process parameters and with or without active cooling. As-built and machined coupons were extracted from different orientations to the print layers and tested. 3D laser scanning was used to accurately capture the geometric properties and surface roughness of the examined WAAM materials. X-ray computed tomography (XCT) scanning was utilised as a non-destructive technique for the detection of porosity. The mechanical properties of the WAAM specimens were obtained from tensile coupon testing assisted by digital image correlation (DIC). Lastly, microstructural analysis was performed to complement the mechanical evaluations. The insights gained from this study will facilitate the understanding of the link between process

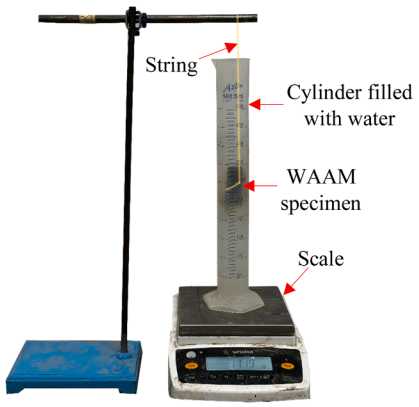


Fig. 5. Density measurement setup.

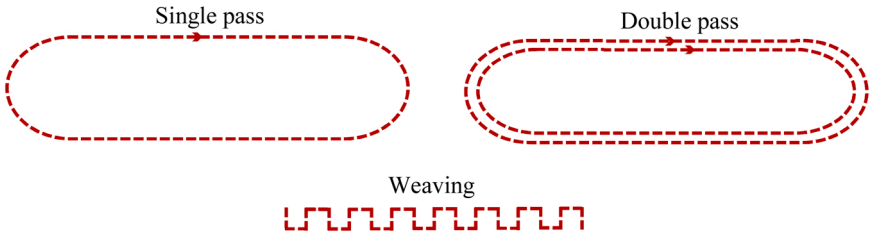


Fig. 3. Illustration of the printing toolpaths.

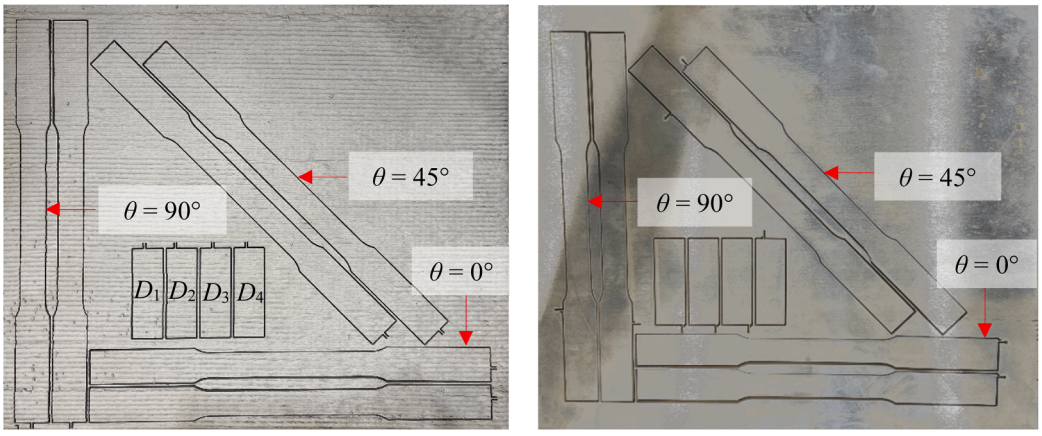


Fig. 4. Orientation of the extracted WAAM coupons from a typical (a) as-built plate and (b) machined plate.

Table 4
Measured densities of examined WAAM steel.

Material ID	ρ (g/cm^3)	ρ/ρ_o
P3.5	7.766	0.9893
P5	7.821	0.9963
P8	7.817	0.9958
P12	7.829	0.9973
A8	7.824	0.9967
A12	7.833	0.9978
WAAM ER110S-G [17]	7.831	0.9975
WAAM ER110S-G [44]	7.830	0.9975
WAAM ER70S-G [57]	7.770	0.9898

parameters and mechanical properties of WAAM steels and aid the development of reliable structural design rules for WAAM steel components, including rules for design by advanced analysis [52,53].

2. Manufacture and preparation of test specimens

Six WAAM steel flat-sided oval tubes with four different nominal thicknesses t_{nom} – 3.5 mm, 5 mm, 8 mm and 12 mm, as shown in Fig. 1, were printed by the Dutch manufacturer MX3D, using a 6-axis ABB robot equipped with a metal inert gas (MIG) welding system, as illustrated in Fig. 2(a). The ovals were printed diagonally (see Fig. 2(a)) on 30 mm-thick, 350 mm × 350 mm steel plates, and were removed from the substrate by flame cutting. Welding wire of grade ER90S-D2 [54] with a nominal diameter of 1.2 mm was employed as the feedstock. The wire diameter was kept constant to enable the influence of different printing strategies on the resulting mechanical properties to be isolated. The chemical composition of the feedstock material and the as-welded mechanical properties, as stated in the wire certificate provided by the manufacturer, are reported in Tables 1 and 2, respectively. The Carbon Equivalent (CE) of the adopted welding wire is equal to 0.63 and 0.43 based on the formulae from AWS D1.1 [55] and EN 1011-2:2001 [56], respectively; note however that these formulae are mainly used for parent metals instead of welding wire. According to AWS 5.28 [54], the adopted welding wire offers overall good weldability and is suitable for both single and multi-pass applications.

The key process parameters for each nominal thickness, including the nominal voltage and current, torch speed, wire feed rate, toolpath etc., are presented in Table 3. The toolpaths selected for printing, i.e. single pass, double pass and weaving, as shown in Fig. 3, are commonly used for the printing of thin-walled elements in practice. Note that the part geometry is expected to somewhat affect the thermal history and the mechanical properties, but this is outside of the scope of the present paper. For the wall thicknesses of 8 mm and 12 mm, two ovals were printed for each thickness, employing either active cooling using compressed air from nozzles arranged in an array along one side of the ovals, or passive (i.e. natural) cooling; see Fig. 2(b). The primary purpose of active cooling was to reduce the dwell time and improve the overall productivity.

To assess the influence of the undulating as-built geometry on the mechanical properties, one of the two WAAM plates extracted from each oval specimen was machined flat. Six tensile coupons, including two repeats at each of the three different orientations $\theta = 0°$, 45° and 90° relative to the print layers, as defined in Fig. 4(a), were extracted by means of water jet cutting, from each plate, leading to 72 tensile coupons in total, along with samples for density measurements and microstructural examination. Finally, the surfaces of the coupons were

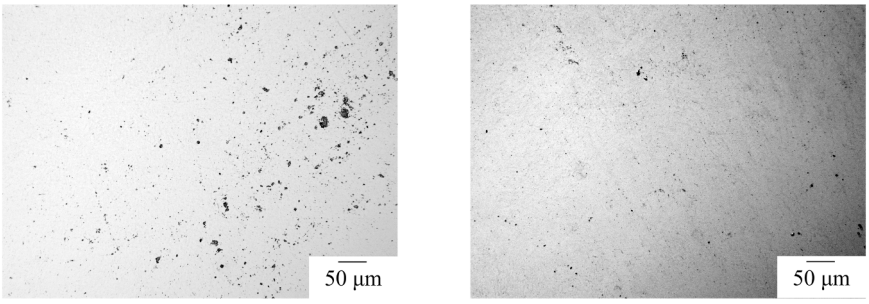


Fig. 6. Typical optical micrographs for (a) P3 and (b) A8 as-polished samples.

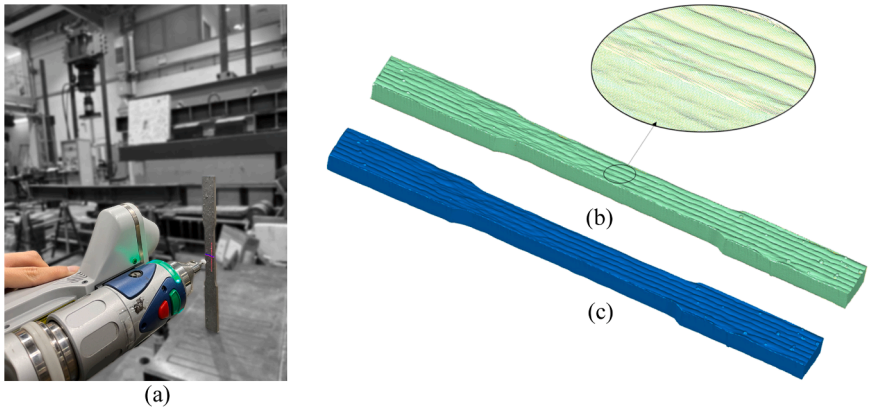


Fig. 7. (a) Laser scanning, (b) point cloud and (c) polygon object of a coupon.

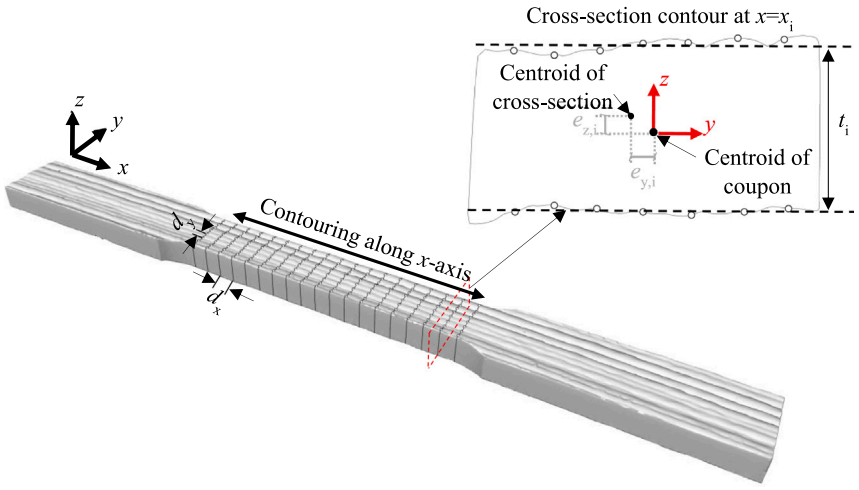


Fig. 8. Determination of coupon geometry in Rhino 3D.

Table 5
Geometric properties of the passively cooled as-built coupons.

Material ID	θ (°)	t (mm)	A (mm^2)	A_{min} / A	A_{sd} / A	e_z (mm)
P3.5	0	3.12	51.0	0.98	0.010	0.40
	0	3.17	51.6	0.97	0.021	0.38
	45	3.19	52.9	0.96	0.017	0.51
	45	3.23	54.2	0.96	0.018	0.43
	90	3.26	53.7	0.96	0.021	0.50
	90	3.23	52.7	0.95	0.024	0.50
P5	0	4.33	71.3	0.97	0.013	0.02
	0	4.35	72.6	0.98	0.010	0.06
	45	4.33	71.8	0.97	0.013	0.15
	45	4.39	72.9	0.98	0.011	0.22
	90	4.51	74.6	0.92	0.024	0.76
	90	4.54	74.7	0.93	0.025	0.78
P8	0	8.17	133.6	0.99	0.006	0.17
	0	7.44	121.2	0.98	0.006	0.08
	45	7.42	121.4	0.97	0.015	0.23
	45	7.46	121.6	0.97	0.016	0.22
	90	7.69	125.7	0.94	0.025	0.32
	90	7.79	127.1	0.94	0.028	0.33
P12	0	11.42	187.1	0.97	0.025	0.07
	0	11.15	181.4	0.98	0.007	0.08
	45	11.08	183.9	0.94	0.019	0.16
	45	11.07	180.7	0.97	0.014	0.15
	90	11.47	187.0	0.92	0.023	0.21
	90	11.45	187.9	0.91	0.024	0.26

sandblasted with cutting sand for waterjetter to remove any welding soot arising from the WAAM process. A visual comparison between the as-built and machined surfaces is presented in Figs. 4(a) and 4(b).

The label of each coupon specimen begins either with an 'A' (active cooling) or a 'P' (passive cooling). The first number is the nominal thickness t_{nom} (in mm), followed by the angle θ (in °) between the orientation of the coupon and the print layers. Finally, 1 or 2 represent the repeated test ID, and M or AB corresponds to the surface condition - machined or as-built, respectively. For example, P3.5-0-1-AB is a coupon specimen extracted from a nominally 3.5 mm-thick, passively cooled and as-built plate at an angle of $\theta = 0°$ to the print layer orientation.

Table 6
Geometric properties of the actively cooled as-built coupons.

Material ID	θ (°)	t (mm)	A (mm^2)	A_{min} / A	A_{sd} / A	e_z (mm)
A8	0	7.84	130.5	0.99	0.005	0.05
	0	7.66	126.4	0.99	0.004	0.03
	45	7.85	128.6	0.93	0.028	0.06
	45	7.89	128.5	0.93	0.025	0.05
	90	7.87	128.3	0.92	0.039	0.10
	90	7.92	129.7	0.91	0.038	0.20
A12	0	11.68	189.2	0.98	0.010	0.05
	0	11.65	188.8	0.97	0.012	0.13
	45	11.53	187.8	0.98	0.010	0.10
	45	11.56	189.9	0.98	0.013	0.08
	90	12.01	196.1	0.92	0.022	0.16
	90	12.09	198.7	0.94	0.022	0.19

3. Density, geometric properties and surface roughness

The density of the WAAM steel and the geometric characteristics of the as-built tensile coupons were examined prior to testing. Archimedes' law was used for the density measurements. To capture the undulating surface geometry of the as-built coupons, advanced 3D laser scanning was employed, and the key geometric properties as well as the surface roughness, were quantitatively determined.

3.1. Density measurements

Density measurements were conducted using Archimedes' principle prior to geometric measurements, not only to determine the material density but also to verify the accuracy of the 3D laser scan data, as discussed in the following subsection. Four representative samples, D_1 to D_4, as shown in Fig. 4(a), were extracted from each type of as-built plate, and the density was measured using the setup presented in Fig. 5; the adopted scale had an accuracy of 0.001 g. Table 4 presents the measured values of the density ρ of the test material, together with the measurements on similar WAAM carbon steel reported by Weber et al. [44], Huang et al. [17] and Al-Nabulsi et al. [57], for comparison purposes. Overall, the measured density of WAAM steel has been shown to be very marginally lower than the standard value for conventional carbon steel $\rho_0 = 7.85$ g/cm^3, which is likely due to the presence of a higher level of porosity in these printed materials, as also observed in Al-Nabulsi et al. [57]. The plates examined herein with a nominal thickness $t_{nom} = 3.5$ mm exhibited the lowest density; optical microscopy using an Olympus BX51 microscope revealed more pores in samples extracted from the 3.5 mm-thick plate compared with the other thicknesses – see Fig. 6.

3.2. Geometric analysis

Advanced 3D laser scanning was employed to digitally capture the undulating surface geometry of the as-built coupons. A Faro ScanArm, integrated with a FARO laser line probe, able to capture up to 500,000 points per second with an accuracy of 0.1 mm and a resolution of 0.075 mm, was utilised for this purpose – see Fig. 7(a). The scan data of

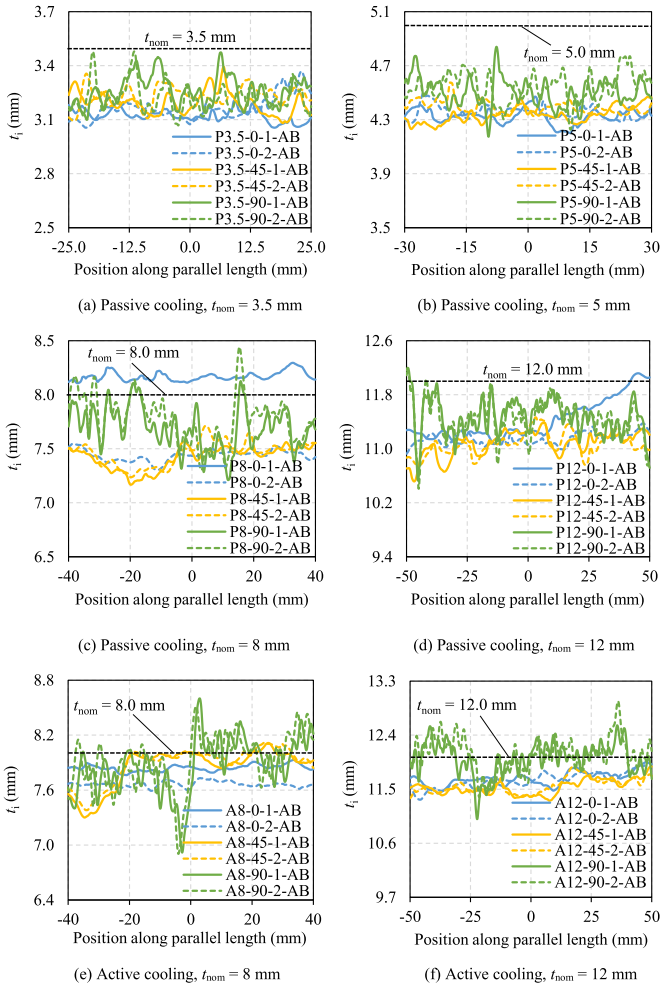


Fig. 9. Thickness variation along parallel length of as-built coupon specimens.

each coupon were converted from a point cloud to a polygonal mesh using the software Geomagic Wrap [58] – see Figs. 7(b) and 7(c). The accuracy of the scan data was verified by comparing the volume of the coupon based on the measured weight and density with the volume of the polygonal mesh, where the difference was shown to be consistently less than 1%.

The processed scan data were imported as an STL file into Rhino 3D [59] for further geometric analysis. For each coupon, the 3D model of the specimen was reoriented in Rhino using principal component analysis. The overall centroid of the coupon model was fixed to the global origin, and the longitudinal axis of the coupon was aligned with the global x-axis. The 3D model was then contoured at a predetermined interval equal to 0.1 mm [28] along the longitudinal axis (x-axis) in order to obtain the geometric properties of each cross-sectional contour – see Fig. 8. The cross-sectional area A_i and the deviation between the centroid of each cross-section contour and the overall centroid along the z-axis, labelled as $e_{z,i}$, were subsequently determined. Moreover, the cross-sectional thickness t_i of each contour i was defined as the average distance between all opposing cross-sectional grid points – see Fig. 8.

The derived geometric properties of the as-built coupons are presented in Tables 5 and 6 for those with passive and active cooling, respectively, where A, A_{min}, A_{sd} represent the mean, minimum and standard deviation values of the cross-sectional area, t is the average thickness of each coupon, and finally e_z is the average of the absolute values of the eccentricities $e_{z,i}$ in the z-direction.

Fig. 9 shows the variation in average thickness t_i along the parallel length of all as-built coupons. The variation of the thickness depends on the orientation of the coupon specimens relative to the print layer orientation θ. As expected, coupons extracted with $\theta = 90°$ presented the highest level of thickness variation along their length due to the surface undulations. This trend is also observed in Tables 5 and 6, where the ratio of A_{min}/A generally decreased for coupons with higher θ, whereas the eccentricities along z-axis generally increased by increasing θ. The as-built surface finishes associated with different process parameters and cooling methods were visually different, as shown in Fig. 10; the surface roughness of the examined WAAM steels is discussed further in Section 3.3.

3.3. Roughness of the as-built surfaces

The surface roughness of the examined WAAM steels, arising primarily from the layer-by-layer nature of the printing, is examined herein using the 3D scan data obtained from the as-built coupons. To isolate roughness within the 3D scan data, it is essential to first remove both the inherent error of form and the waviness of the coupons, as shown in Fig. 10. Error of form, in this case, out-of-flatness, is often present due to imperfections such as layer shifts or thermal distortions and may influence the structural behaviour of the element. Waviness, on the other hand, pertains to variations in the thickness of the WAAM part that result from inconsistencies in the deposition process [60,61].

The out-of-flatness profile was determined as the centroid of each pair of opposing grid points, and was eliminated by subtracting the z-coordinate of the centroid $z_{i,c}$ from those of the corresponding surface grid points $z_{i,1}$ and $z_{i,2}$ – see Fig. 11(a). Subsequently, the waviness of each coupon surface was obtained by applying a moving average filter to smoothen the surface profile, with a filtering window size such that the surface undulations were retained, as shown in Fig. 11(b). To determine the appropriate filtering window size, expressed as the product of the layer height and a factor α, a sensitivity study was conducted, as shown in Fig. 12(a), where the roughness parameter S_z, as defined later in this section, is plotted against different α values. Errors may arise when there is a localised abrupt change in the layer width (i.e. the wall thickness), which may not be captured correctly by the adopted filtering method. It can be seen in Fig. 12 that increasing the factor α leads to an increase in the roughness parameter S_z, up to approximately $\alpha = 7$ for all six

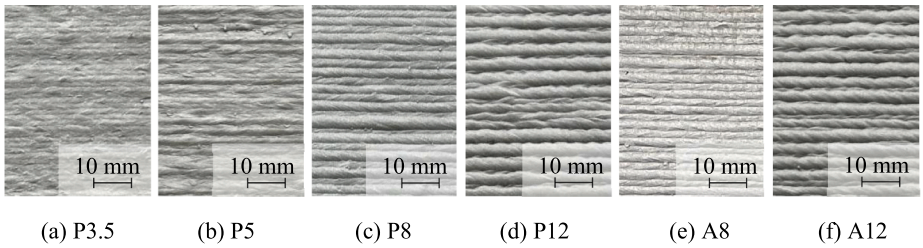


Fig. 10. Comparison of surface finish of as-built specimens.

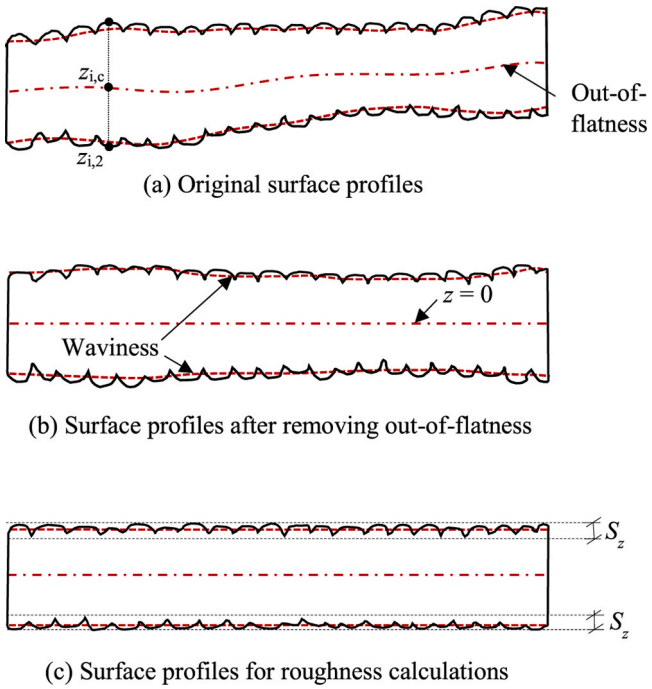


Fig. 11. Definition of (a) out of-flatness, (b) waviness, and (c) roughness.

different WAAM coupon types, as illustrated in Fig. 12(b), beyond which the derived roughness values remain relatively constant. Therefore, a filtering window size corresponding to $\alpha = 7$ was used to determine the waviness. The waviness profile was eliminated from the scan data in a similar manner to the out-of-flatness by modifying the z-coordinates of the scan data, as illustrated in Fig. 11(c). Fig. 13 shows the scan data processing steps ((1)-(4)) for a typical examined surface for roughness analysis.

Following the guidelines in EN ISO 25178-2:2022 [60], the filtered surface profiles were evaluated using several parameters to describe the unevenness of the surface, including the maximum height S_z:

$$S_z = z_{max}(x,y) - z_{min}(x,y) \tag{1}$$

the arithmetic mean height S_a:

$$S_a = \frac{1}{\tilde{A}}\iint_{\tilde{A}} |z(x,y)|\mathrm{d}x\mathrm{d}y \tag{2}$$

the root mean square height S_q:

$$S_q = \sqrt{\frac{1}{\tilde{A}}\iint_{\tilde{A}} z^2(x,y)\mathrm{d}x\mathrm{d}y} \tag{3}$$

the skewness S_{sk}:

$$S_{sk} = \frac{1}{S_q^3}\left(\frac{1}{\tilde{A}}\iint_{\tilde{A}} z^3(x,y)\mathrm{d}x\mathrm{d}y\right) \tag{4}$$

and the kurtosis S_{ku}:

$$S_{sk} = \frac{1}{S_q^4}\left(\frac{1}{\tilde{A}}\iint_{\tilde{A}} z^4(x,y)\mathrm{d}x\mathrm{d}y\right) \tag{5}$$

The x and y coordinates describe the longitudinal and transverse directions of the surface, respectively, while z represents the direction normal to the surface. The term $\tilde{A}$ refers to the examined surface, i.e. the parallel length of the coupons. A contour spacing of 0.1 mm was employed along both the x and y-axes, consistent with the geometric analysis presented earlier, to balance accuracy and computational efficiency.

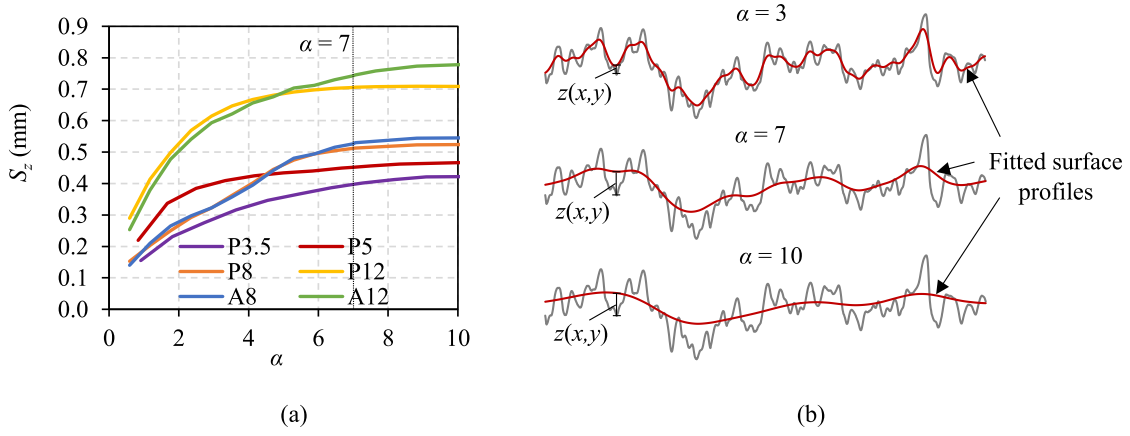


Fig. 12. (a) Comparison of the maximum height S_z with the smoothening factor α and (b) fitted surface profile according to different smoothening factors α.

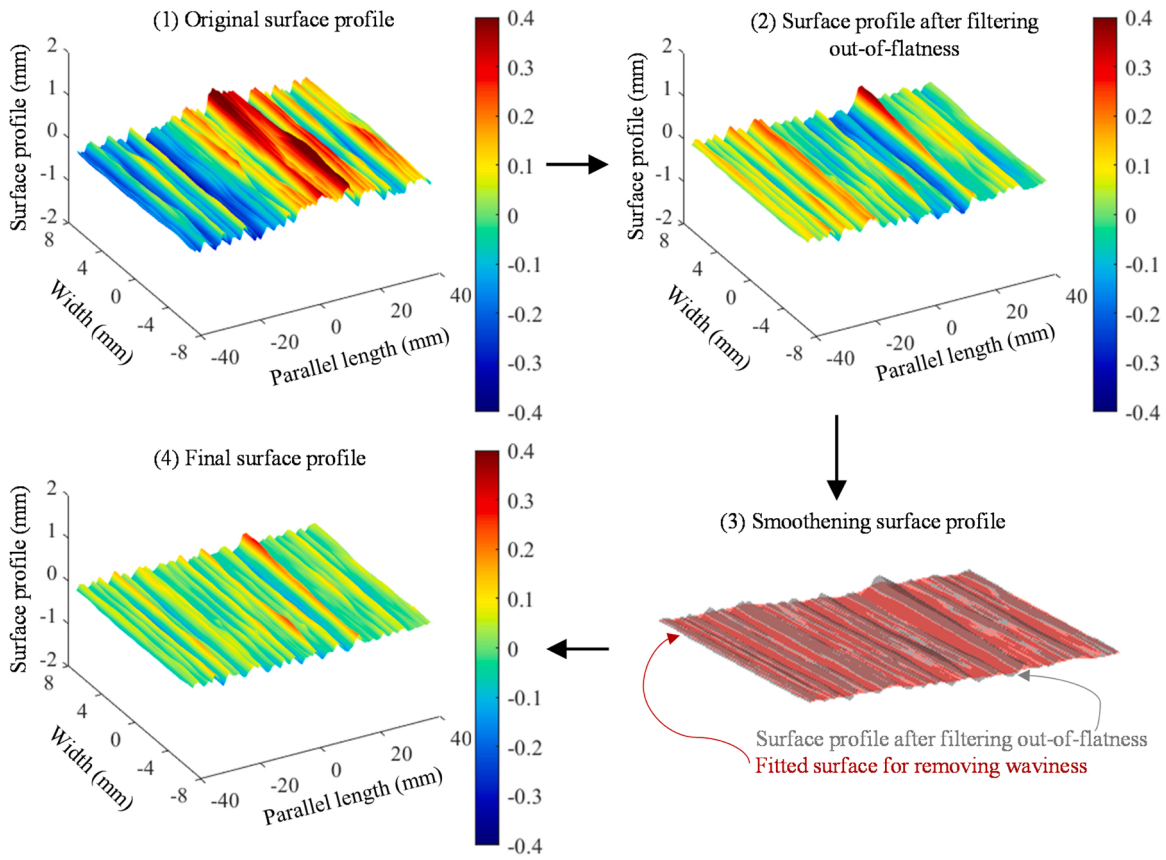


Fig. 13. Illustration of the applied steps ((1) - (4)) for smoothening the surface profiles for roughness evaluation.

Table 7
Roughness properties of the as-built plates.

Material ID	S_z (mm)	S_a (mm)	S_q (mm)	S_{sk}	S_{ku}
P3.5	0.403	0.033	0.042	0.134	3.339
P5	0.464	0.039	0.049	0.061	3.367
P8	0.502	0.057	0.069	−0.065	2.879
P12	0.724	0.076	0.082	−0.203	3.311
A8	0.523	0.062	0.070	−0.108	2.909
A12	0.722	0.080	0.083	−0.062	3.134

Table 7 provides the derived surface roughness parameters, averaged from the results for all as-built coupons, for the examined WAAM materials with different printing strategies. As the thickness increases from 3.5 mm to 12 mm, there is an increasing trend for the maximum height S_z, the mean arithmetic height S_a and the mean square height S_q, which suggests that the thicker plates exhibited greater surface height variations (i.e. more pronounced surface roughness). This can be attributed to the fact that the ovals with 8 mm and 12 mm thicknesses were produced using different toolpaths, i.e. double pass and weaving respectively, as shown in Fig. 3, which affected the surface roughness. Furthermore, the surface roughness has previously be found to also be affected by the layer height and weld pool geometry and stability, which are linked to the wire feed rate, the travel speed and heat input [62]; further investigations on this topic are needed to understand this correlation better. The maximum height S_z, the mean arithmetic height S_a and the mean square height S_q for each tensile specimen are plotted against thickness in Fig. 14(a)–(c), where the results for coupons with the same printing strategy are shown to be rather consistent and the increasing trend of surface roughness with increasing thicknesses is clear. The cooling method is seen to have negligible influence on the surface texture. The skewness S_{sk} values for the 8 mm and 12 mm plates are negative, indicating left-skewed distributions, where more surface heights fall below the mean. In contrast, the 3.5 mm and 5 mm plates show positive skewness, suggesting right-skewed distributions, where surface heights predominantly lie above the mean. Finally, the kurtosis S_{ku} values also vary with thickness; the 8 mm plates exhibit the lowest values of S_{ku}, equal to 2.879 and 2.909, which are less than 3, indicating a less pronounced tail compared to a normal distribution. Conversely, the kurtosis values of the remaining plate thicknesses are above 3, implying a slightly more pronounced tail.

4. Defect examinations

To facilitate the qualification and wider adoption of WAAM in practice, knowledge and control of printing defects are essential. Non-destructive testing (NDT) enables the detection and assessment of defects in materials without compromising their usability [48,57,63]. In the present study, X-ray computed tomography (XCT), a common NDT method for metallic components, was used to inspect the quantitative distribution of pores in a selected group of WAAM steel specimens with nominal thicknesses of 8 mm and 12 mm.

4.1. XCT setup

XCT was used to scan the machined coupons associated with the nominal print thicknesses of 8 mm and 12 mm and both active and passive cooling. A 320 kV CT scanner was used to examine the internal defects. The interior of the equipment is depicted in Fig. 15 which shows the X-ray generator, which has its output port covered by a copper filter to limit the X-ray wavelength. A Styrofoam jig, transparent to X-rays, was placed on the central turntable to hold the specimen. Two images per degree of rotation were captured to enhance the contrast.

4.2. XCT results

The software myVGL [64] was utilised to analyse the captured images. The CT scan results revealed a high level of localised pores in Specimens P8-45-1-M, P8-45-2-M, P8-90-2-M and A12-90-2-M. Typical XCT results are displayed in Figs. 15 and 16 for Specimens P8-45-2-M and A12-90-2-M respectively. Figs. 16(a) and 17(a) illustrate the distributions of the porosity, calculated as the volume fraction of pores at 1 mm intervals, along the parallel length of the coupons. Figs. 16(b) and 17(b) are the CT scans of the coupons, showing the distribution of pores; the locations at which the coupons fractured are shown in Figs. 16(c) and 17(c) and correspond to the areas with the highest concentration of pores. Figs. 16(d) and 17(d) depict the fracture surfaces of both coupons, where a high degree of porosity was revealed. The XCT results did not show any noticeable influence from the process parameters, wall thickness and cooling method on the level of defects; instead, the porosity was highly localised and attributable to external conditions /

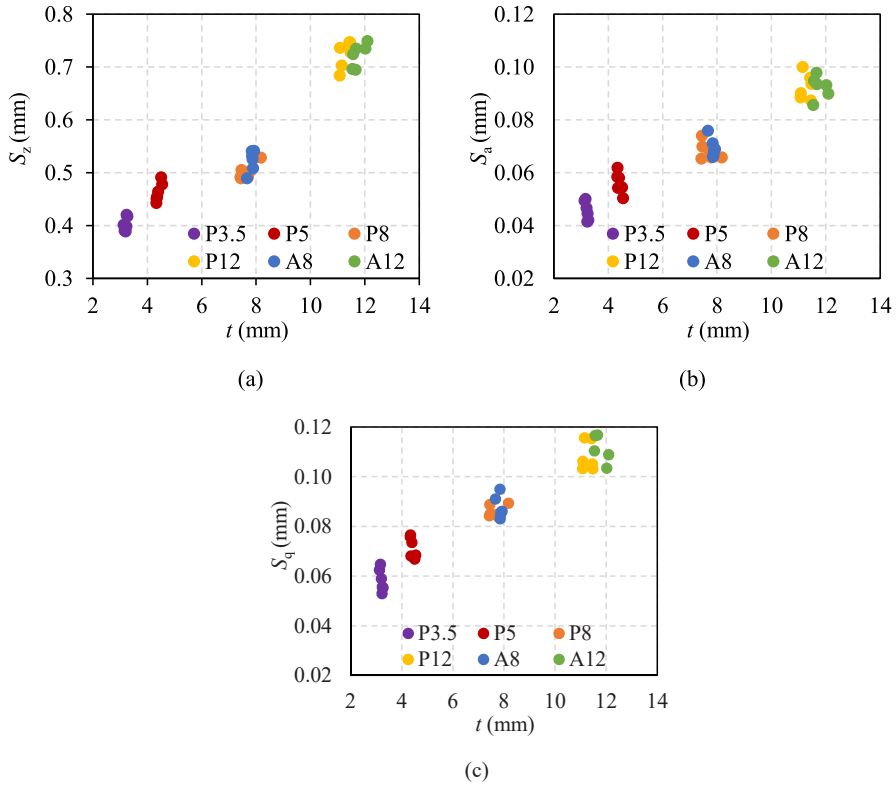


Fig. 14. Comparison of (a) S_z, (b) S_a and (c) S_q with the average thickness t of all the tested tensile specimens.

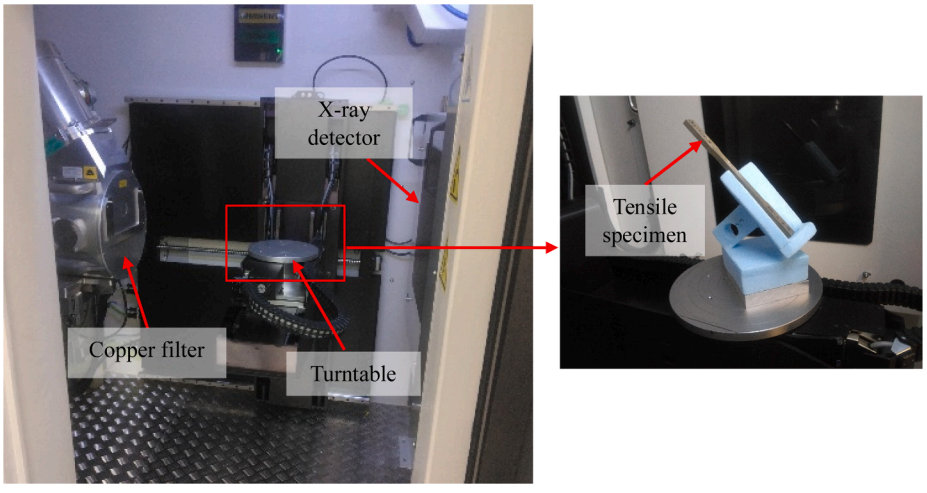


Fig. 15. XCT scanning equipment for examination of defects in WAAM materials.

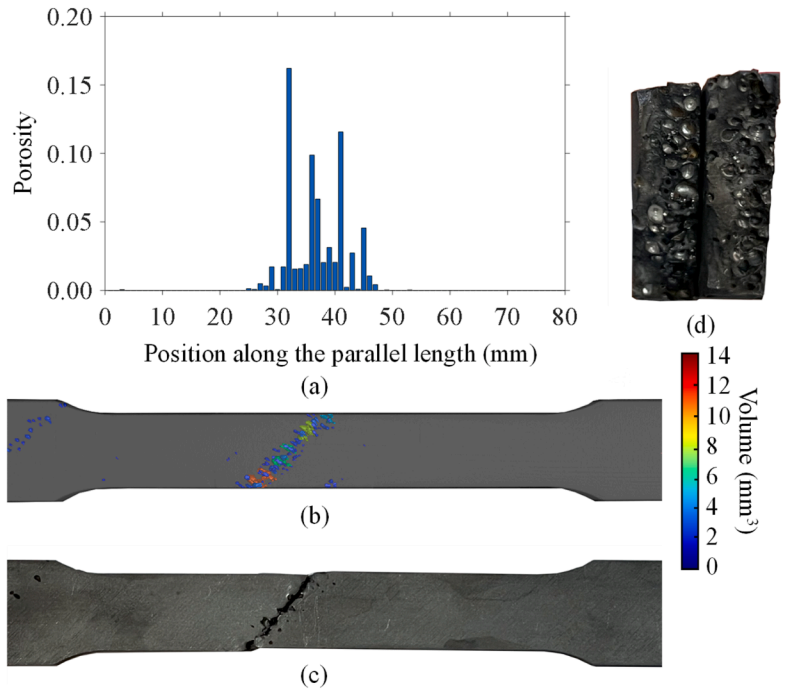


Fig. 16. Specimen P8-45-2-M: (a) Distribution of the volume of pores along the parallel length, (b) illustration of the pore distribution, (c) photo of the fractured tensile coupon and (d) photo of the fracture surface.

human error (e.g. unintentional disturbances of the shielding gas). This could be detected from manufacturing logs [44], and more frequent supervision and intervention could minimise such defects.

5. Tensile coupon testing

The stress-strain behaviour of the WAAM material was investigated via tensile coupon testing. In total, 72 coupon specimens, half with as-built surfaces and half with machined surfaces, were tested. The test programme was performed to investigate the influence of various factors, including the printing strategy and the resulting thickness of the material, the cooling method and the loading direction relative to their print layer orientation, on the mechanical properties.

5.1. Test setup

The test setup used in this study is depicted in Fig. 18. An Instron 8802 250 kN servohydraulic testing machine with hydraulic grips was used for the uniaxial monotonic loading of the coupons. The tests were conducted under displacement control according to EN ISO 6892-

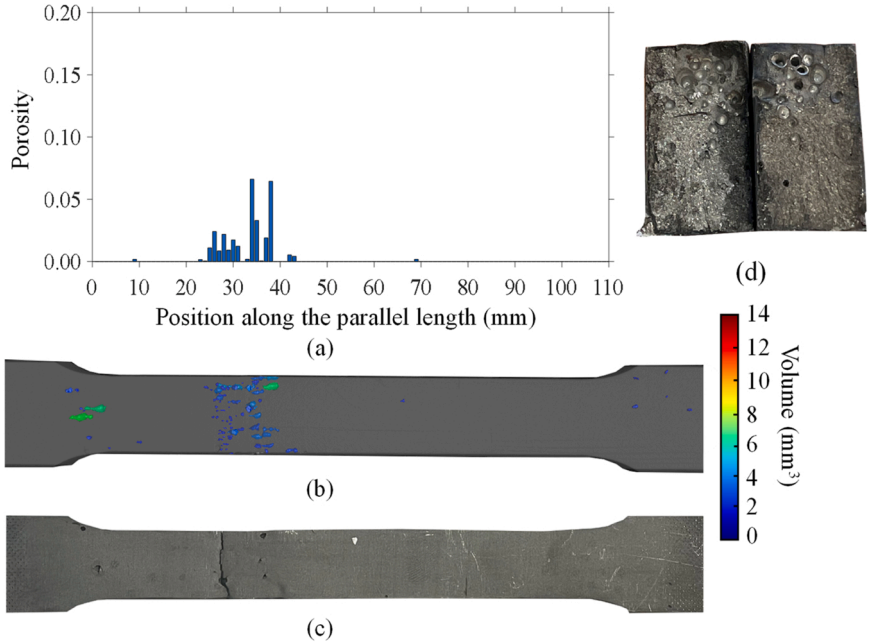


Fig. 17. Specimen A12-90-2-M: (a) Distribution of the pores along the parallel length, (b) illustration of the pore distribution, (c) photo of the fractured tensile coupon and (d) photo of the fracture surface.

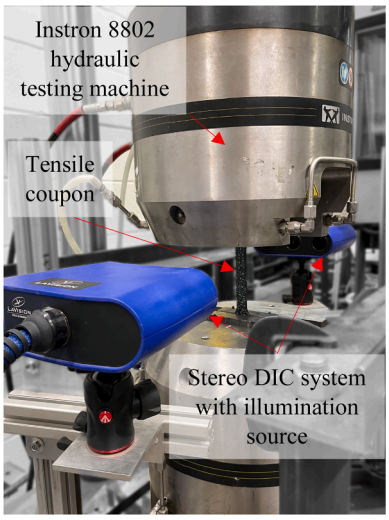


Fig. 18. Test setup for tensile coupon testing.

1:2019 [65]. The displacement rate was set at an equivalent strain rate of 0.00007 s^{-1} up to the 0.2% proof strength, with a gradual increase to a strain rate of 0.00025 s^{-1} beyond the yield strength until fracture. To capture the strain and displacement fields in the parallel length of both sides of the coupon specimens, two LaVision StrainMaster Compact stereo digital image correlation (DIC) systems with an integrated LED illumination source were utilised. Before testing, a random pattern, consisting of a black matt background and white speckles, was applied to the parallel length of both sides of the coupons; matt paint was used to avoid data loss due to reflection during the image capturing. The DIC images were acquired with a 2 Hz frequency and then processed in DaVis 10 [64]. The applied load and the machine displacement were measured and recorded along with the DIC images in DaVis 10 [66]. Finally, the elongation at fracture was determined by marking a set of overlapping standard gauge lengths equal to $5.65\sqrt{A}$ on both sides of the coupons, where A was taken as the mean cross-sectional area of the tensile coupon, as presented in Tables 5 and 6.

5.2. Test results

This section presents the key mechanical properties of the examined WAAM materials obtained from the tensile coupon tests. Figs. 19 and 22 display the stress-strain curves for the machined and as-built coupons, respectively. For the as-built coupons, due to their undulating geometry, the applied stress was calculated based on the mean cross-sectional area of their parallel length A determined by means of laser scanning, as shown previously in Tables 5 and 6, and the presented results should be considered to be 'effective' mechanical properties. For both the as-built and machined coupons, the longitudinal strain was determined via virtual extensometers over the parallel length using the DIC data. Tables 8 and 9 and Figs. 20 and 23 present the key material properties for the machined and as-built tensile coupons, respectively, including the Young's modulus E, the Poisson's ratio ν, the yield strength f_y, the ultimate strength f_u, the strain at the ultimate strength ε_u, the strain at fracture over the standard gauge length ε_f and the strain hardening exponents, n and m_u, of the two-stage Ramberg-Osgood material model [67,68,69]. The Young's modulus E was determined through a least squares analysis of the stress-strain data between approximately 20% and 60% of the yield strength f_y, and the Poisson's ratio ν was computed based on the ratio of the mean transverse to mean longitudinal strains within the elastic range. Finally, the yield strength f_y was taken equal to the 0.2% proof stress in the case where the stress-strain curves had no clearly defined yield point.

5.3. Discussion of test results

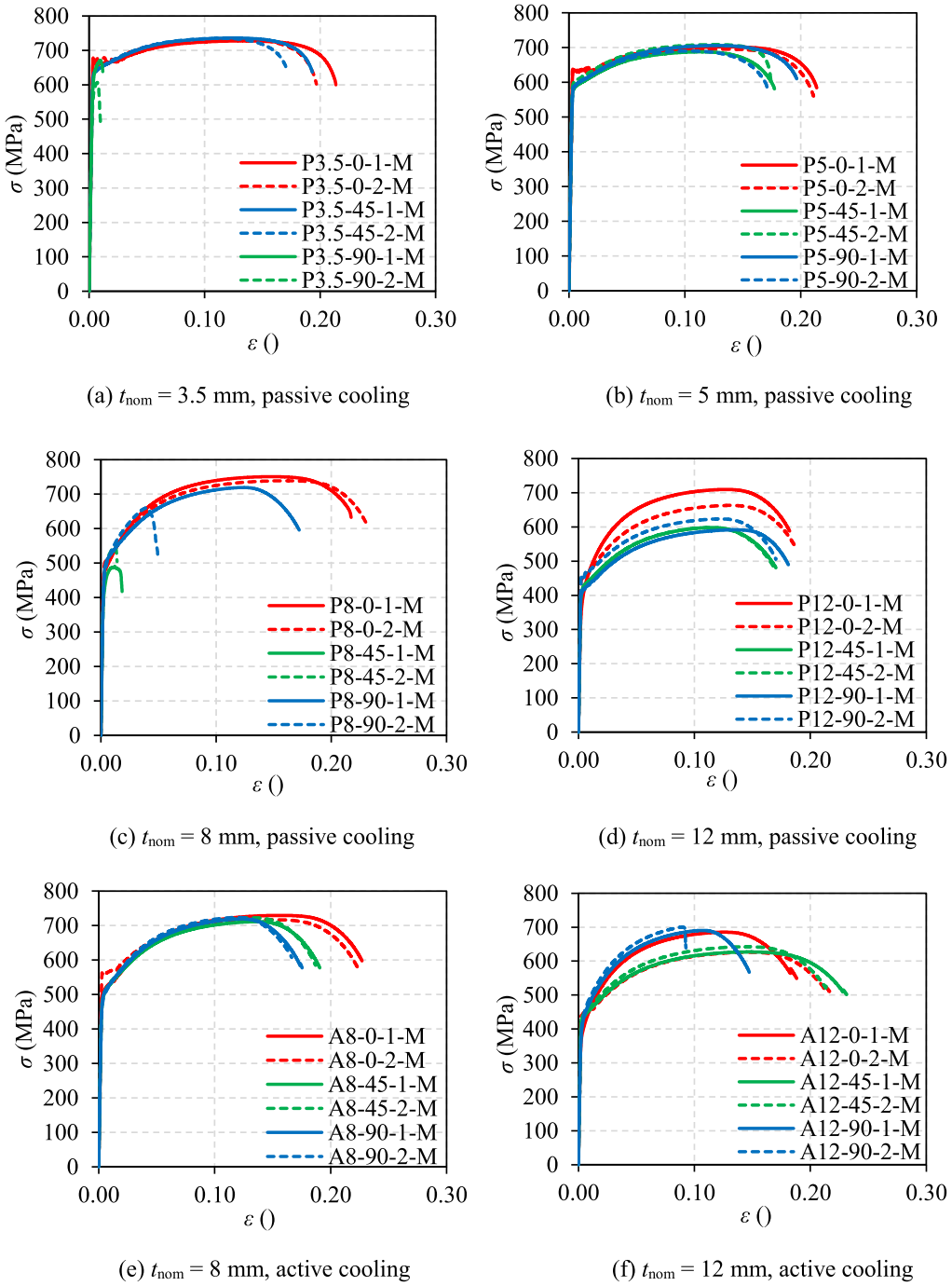
The obtained tensile coupon test results are discussed in this section; note that those coupons with significant porosity, as marked in Tables 8 and 9, are excluded from the discussion to avoid misleading conclusions.

5.3.1. Extent of material anisotropy

The extent of material anisotropy is examined in this subsection based on the machined coupon test results. Fig. 19 illustrates that most of the stress-strain curves for the machined coupons loaded parallel to the print layer orientation (i.e. $\theta = 0°$) resemble typical hot-rolled steels, with a well-defined yield point and a yield plateau followed by strain hardening. On the other hand, the machined coupons with $\theta = 45°$ and 90° to the print layer orientation exhibited more rounded stress-strain behaviour, without a distinct yield point or a yield plateau. The obtained Young's modulus E is shown to be rather consistent for all the machined coupons, as depicted in Fig. 20(a), and falls within the expected range of 200–220 GPa for conventional carbon steels. Similar observations can be made for the Poisson's ratios ν, as shown in Fig. 20(b), revealing the elastic behaviour of the examined WAAM carbon steel to be essentially isotropic. The yield and ultimate strengths f_y and f_u are graphically compared in Figs. 20(c) and 20(d). A slightly higher yield strength f_y was observed at $\theta = 0°$ for the 3.5 mm, 5 mm and 8mm-thick coupons due mainly to the presence of yield plateau, while the ultimate strengths f_u were generally independent of the angle θ to the print layer orientation, except for the 12 mm-thick coupons. As shown in Figs. 19(d) and 19(f), the P12 and A12 specimens exhibited noticeably different stress-strain responses in the strain hardening range for different angles θ. This anisotropic behaviour in the plastic range might be attributed to the variability of individual coupons, and the more complex thermal history due to the adopted weaving toolpath; further work is needed to gain a deeper insight into the cause of such behaviour. The strains at the ultimate stress ε_u and at fracture ε_f, as shown in Figs. 20(e) and 20(f), remain similar across the different orientations. Fig. 21 shows the typical surface strains captured by DIC for three different angles θ shortly before fracture, where it can be observed that, independently of the angle θ, all the machined coupons showed very similar patterns of necking. The fracture of the coupon specimen shown in Fig. 21(c), which had a relatively high cross-section aspect ratio b/t of 5.3 and thus a relatively low average stress triaxiality, was primarily governed by shear, following the direction of maximum shear stress at an inclined angle; in contrast, those with relatively low cross-section aspect ratios, as shown in Fig. 21(a) and (b), tended to experience relatively high average stress triaxialities and thus fractured by void formation and along a line perpendicular to the applied tensile load [70].

5.3.2. Influence of the surface undulations

The influence of the undulating as-built geometry inherent to the WAAM process on the mechanical properties is analysed in this section by comparing the as-built and machined coupon test results. A comparison between Fig. 19 and Fig. 22 shows that the stress-strain curves of the as-built coupons are generally similar to those of the machined coupons, with a distinct yield point typical of carbon steels only present for some of the coupons with $\theta = 0°$. Generally, the stress-strain responses of the as-built coupons was slightly more rounded compared to their machined counterparts, particularly the as-built coupons with $\theta = 90°$ as a result of the earlier stiffness loss due to the undulating geometry. The effective material properties of the as-built coupons, averaged for each angle relative to the print layer orientation and indicated by the subscript "eff", and normalised by the corresponding properties of their machined counterparts, are plotted in Fig. 26. For the Young's modulus E, the undulating geometry had the most significant effect on the as-built coupons with $\theta = 90°$, whereas no significant influence was observed on the Poisson's ratios ν, as depicted in Figs. 26(a) and 26(b) respectively. In Figs. 26(c) and 26(d), the as-built coupons showed a 6% and a 3% decrease on average in yield strength f_y and ultimate strength



(a) t_{nom} = 3.5 mm, passive cooling

(b) t_{nom} = 5 mm, passive cooling

(c) t_{nom} = 8 mm, passive cooling

(d) t_{nom} = 12 mm, passive cooling

(e) t_{nom} = 8 mm, active cooling

(f) t_{nom} = 12 mm, active cooling

Fig. 19. Stress-strain curves of machined coupons.

Table 8
Material properties of machined tensile coupon specimens.

Specimen ID	E (MPa)	ν	f_y (MPa)	f_u (MPa)	ε_u	ε_f	f_u/f_y	$\varepsilon_u/\varepsilon_y$	n	m_u
P3.5-0-1-M	213605	0.27	665	728	0.13	0.21	1.09	66.70	32.20	1.75
P3.5-0-2-M	209971	0.27	670	733	0.12	0.20	1.09	59.87	20.40	1.53
P3.5-45-1-M	210381	0.29	639	736	0.12	0.20	1.15	61.46	19.38	1.96
P3.5-45-2-M	210678	0.28	636	735	0.12	0.17	1.16	57.59	16.68	1.93
P3.5-90-1-M*	214073	0.27	637	671	0.01	0.01	1.05	4.98	17.03	2.01
P3.5-90-2-M*	204042	0.28	594	607	0.01	0.01	1.02	3.59	14.79	2.16
P5-0-1-M	207816	0.27	634	702	0.13	0.22	1.11	65.36	20.40	1.94
P5-0-2-M	204182	0.28	626	696	0.13	0.21	1.11	64.68	31.51	1.52
P5-45-1-M	209471	0.28	583	688	0.11	0.18	1.18	57.19	29.06	2.15
P5-45-2-M	215207	0.28	601	709	0.13	0.18	1.18	63.90	27.29	2.36
P5-90-1-M	214210	0.29	589	706	0.13	0.20	1.20	62.67	24.25	1.88
P5-90-2-M	211210	0.28	589	691	0.11	0.17	1.17	53.16	9.36	1.70
P8-0-1-M	219158	0.27	483	751	0.15	0.22	1.55	73.15	18.75	3.23
P8-0-2-M	216786	0.29	507	739	0.16	0.23	1.46	81.38	35.10	3.51
P8-45-1-M*	204771	0.30	447	490	0.01	0.02	1.10	5.88	20.40	2.49
P8-45-2-M*	212001	0.28	496	548	0.01	0.01	1.11	6.18	20.47	2.67
P8-90-1-M	204714	0.29	492	747	0.12	0.17	1.52	59.90	10.58	1.75
P8–90–2-M*	204212	0.28	488	660	0.04	0.05	1.35	19.33	13.30	1.87
P12-0-1-M	214756	0.28	396	710	0.13	0.18	1.79	62.75	7.91	3.41
P12-0-2-M	216440	0.28	452	663	0.13	0.19	1.47	66.20	20.40	2.54
P12-45-1-M	216610	0.29	425	598	0.11	0.17	1.41	56.45	12.30	2.25
P12-45-2-M	209726	0.28	418	598	0.11	0.17	1.43	56.53	13.05	2.38
P12-90-1-M	217005	0.29	418	592	0.13	0.18	1.42	67.03	7.30	2.69
P12-90-2-M	218712	0.27	456	624	0.12	0.17	1.37	61.18	11.76	2.86
A8-0-1-M	218653	0.28	508	730	0.16	0.23	1.44	78.33	12.91	3.17
A8-0-2-M	217931	0.28	559	719	0.15	0.22	1.29	74.15	20.40	1.63
A8-45-1-M	215413	0.29	498	711	0.14	0.19	1.43	67.60	11.16	2.49
A8-45-2-M	218242	0.29	501	723	0.14	0.19	1.44	67.60	14.40	2.57
A8-90-1-M	213057	0.27	501	719	0.12	0.17	1.44	61.57	11.62	2.62
A8-90-2-M	210426	0.28	492	724	0.12	0.17	1.47	60.43	11.83	2.44
A12-0-1-M	208858	0.29	393	685	0.12	0.19	1.74	62.15	20.40	2.29
A12-0-2-M	210780	0.28	446	626	0.15	0.22	1.40	73.68	16.57	4.05
A12-45-1-M	211859	0.29	436	627	0.15	0.23	1.44	74.60	18.19	2.99
A12-45-2-M	210815	0.30	440	642	0.15	0.21	1.46	73.47	16.97	2.53
A12-90-1-M	204924	0.28	423	691	0.11	0.15	1.63	54.00	14.99	2.31
A12-90-2-M*	210016	0.28	426	701	0.09	0.09	1.64	44.66	9.95	2.01

*Tensile coupons with significant porosity within their parallel length

Table 9
Material properties of as-built tensile coupon specimens.

Specimen ID	E (MPa)	ν	f_y (MPa)	f_u (MPa)	ε_u	ε_f	f_u/f_y
P3.5-0-1-AB	204629	0.27	652	728	0.14	0.22	1.12
P3.5-0-2-AB	203728	0.27	644	713	0.13	0.18	1.11
P3.5-45-1-AB*	202191	0.30	621	716	0.11	0.14	1.15
P3.5-45-2-AB*	200576	0.27	612	707	0.11	0.12	1.16
P3.5-90-1-AB*	194588	0.26	593	655	0.03	0.03	1.10
P3.5-90-2-AB*	194081	0.26	582	694	0.07	0.07	1.19
P5-0-1-AB	203589	0.27	646	704	0.12	0.23	1.09
P5-0-2-AB	206345	0.27	623	698	0.13	0.19	1.12
P5-45-1-AB	207857	0.28	569	682	0.11	0.15	1.20
P5-452-AB	206581	0.29	569	685	0.14	0.20	1.20
P5-90-1-AB	189316	0.28	550	654	0.09	0.10	1.19
P5-90-2-AB	191986	0.27	538	619	0.05	0.06	1.15
P8-0-1-AB	212642	0.28	457	709	0.14	0.20	1.55
P8-0-2-AB	209608	0.27	475	697	0.14	0.20	1.47
P8-45-1-AB	205757	0.28	487	684	0.09	0.10	1.41
P8-45-2-AB	204789	0.27	481	683	0.10	0.16	1.42
P8-90-1-AB*	195864	0.29	472	593	0.03	0.04	1.26
P8-90-2-AB*	197797	0.28	470	622	0.04	0.04	1.32
P12-0-1-AB	204384	0.28	377	640	0.11	0.18	1.70
P12-0-2-AB	210011	0.29	415	616	0.14	0.21	1.48
P12-45-1-AB	206103	0.29	381	566	0.11	0.15	1.49
P12-45-2-AB	204450	0.28	382	571	0.13	0.17	1.50
P12-90-1-AB	197263	0.28	385	613	0.12	0.15	1.59
P12-90-2-AB	193341	0.28	382	601	0.11	0.15	1.57
A8-0-1-AB	208539	0.29	455	730	0.15	0.23	1.60
A8-0-2-AB	211651	0.27	540	705	0.15	0.23	1.31
A8-45-1-AB	207133	0.28	465	680	0.11	0.15	1.46
A8-45-2-AB	204097	0.28	469	685	0.11	0.13	1.46
A8-90-1-AB	204618	0.27	456	682	0.11	0.13	1.50
A8-90-2-AB	203730	0.28	453	674	0.09	0.10	1.49
A12-0-1-AB	212587	0.28	418	606	0.15	0.21	1.45
A12-0-2-AB	203923	0.30	379	646	0.12	0.18	1.71
A12-45-1-AB	203218	0.29	404	623	0.14	0.19	1.54
A12-45-2-AB	200858	0.29	398	596	0.09	0.09	1.50
A12-90-1-AB*	197509	0.28	395	596	0.06	0.06	1.51
A12-90-2-AB*	193261	0.29	392	571	0.04	0.05	1.46

*Tensile coupons with significant porosity within their parallel length

f_u, respectively, compared to the machined coupons. The as-built coupons with $\theta = 90^\circ$ again showed the highest average reduction in both yield f_y and ultimate strength f_u of more than 7%, with fracture generally occurring at the minimum cross-section, as depicted in Fig. 25. Regarding the strain at the ultimate stress ε_u and the strain at fracture ε_f, the average ratios $\varepsilon_{u,eff}/\varepsilon_u$ and $\varepsilon_{f,eff}/\varepsilon_f$ are equal to 0.91 and 0.83 respectively, and a clear variation in ε_u and ε_f can be seen in the as-built coupons tested at different angles θ, as shown in Figs. 23(e) and 23(f). By analysing the typical DIC surface strains shown in Fig. 24, it is revealed that the strain fields in the as-built coupons are somewhat non-uniform due to their undulating geometry, and the coupons with $\theta = 90^\circ$ exhibit notably higher strain concentrations compared with the other orientations as a result of the accumulation of deformations in the troughs of the undulating surfaces, and thus lower ultimate and fracture strains. Finally, Fig. 27 illustrates that the higher the ratio A_{min}/A, generally the lower the ratios of E_{eff}/E, $f_{y,eff}/f_y$ and $f_{u,eff}/f_u$ become.

5.3.3. Influence of active cooling

As discussed in Section 2, two ovals with nominal thicknesses of 8 mm and 12 mm were printed using both active and passive cooling methods to investigate their impact on the material properties. Comparing the results from the machined coupon tests in Fig. 20, the 12 mm-thick actively cooled specimens with $\theta = 90^\circ$ exhibited higher ultimate strengths compared to the passively cooled counterparts. Additionally, the elongation of the 12 mm-thick actively cooled specimens with $\theta = 45^\circ$ was greater than that of the corresponding passively cooled specimens. Although these differences are evident, no clear trend was observed based on the limited dataset, and further studies are needed.

5.3.4. Influence of thickness

The influence of the printed wall thickness on the mechanical properties associated with both the as-built and machined surface finishes is discussed in this section. It should be noted that the influence of wall thickness is primarily a result of the change in printing parameters leading to different heat inputs and cooling rates. The key mechanical properties are averaged for each different thickness independently of the cooling method (which has been shown in Section 5.3.3 to have had negligible influence on the studied coupons) and the angle θ to the printing layer orientation, and are plotted against the as-built wall thickness in Fig. 28. The Young's modulus E and the Poisson's ratio ν remain relatively constant across the thickness range for both the machined and as-built coupons, while the yield strength f_y and the ultimate strength f_u are shown to vary with the wall thickness. The yield strength f_y shows a clear drop with increasing thickness for both the as-built and machined samples. This is attributed to the different microstructure between the coupons with different thicknesses and is analysed thoroughly in Section 6. The ultimate strength f_u also decreases slightly with increasing thickness for both the machined and as-built coupons with the exception of the 8 mm-thick specimens. In addition, strain hardening was less pronounced in the coupons with smaller thicknesses, as reflected by the f_u/f_y values in Table 8, where the machined coupons with nominal thicknesses of 3.5 mm and 5 mm have an average ratio of f_u/f_y equal to 1.14, while those with nominal thicknesses of 8 mm and 12 mm have an average ratio f_u/f_y equal to 1.48. Finally, no clear trend is observed for the percentage in elongation at the ultimate stress ε_u and at fracture ε_f.

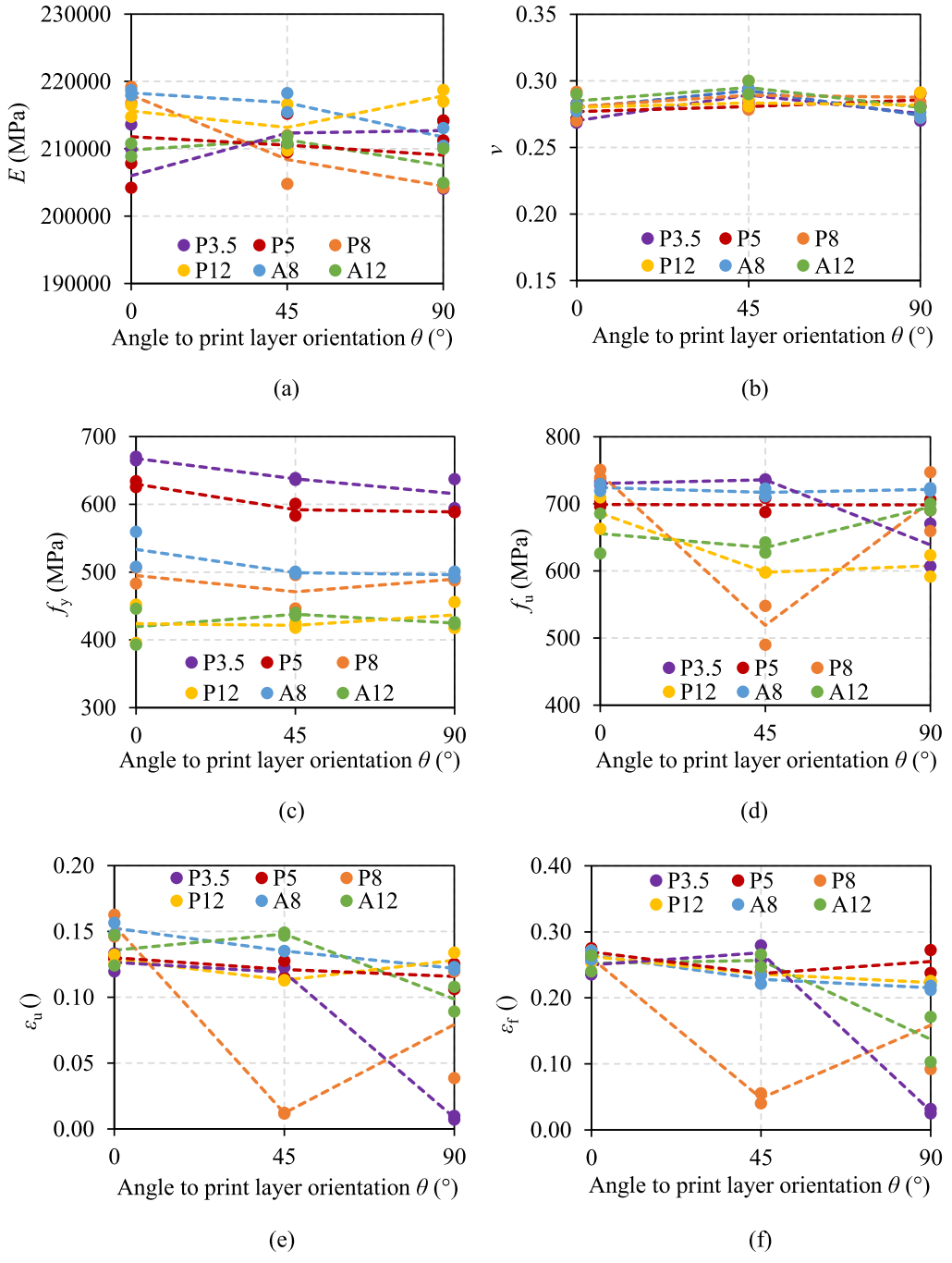


Fig. 20. (a) Young's Modulus E, (b) Poisson's ratio ν, (c) yield strength f_y, (d) ultimate strength f_u, (e) elongation at ultimate strength ε_u and (f) elongation at fracture ε_f at different angles θ of machined tensile coupons.

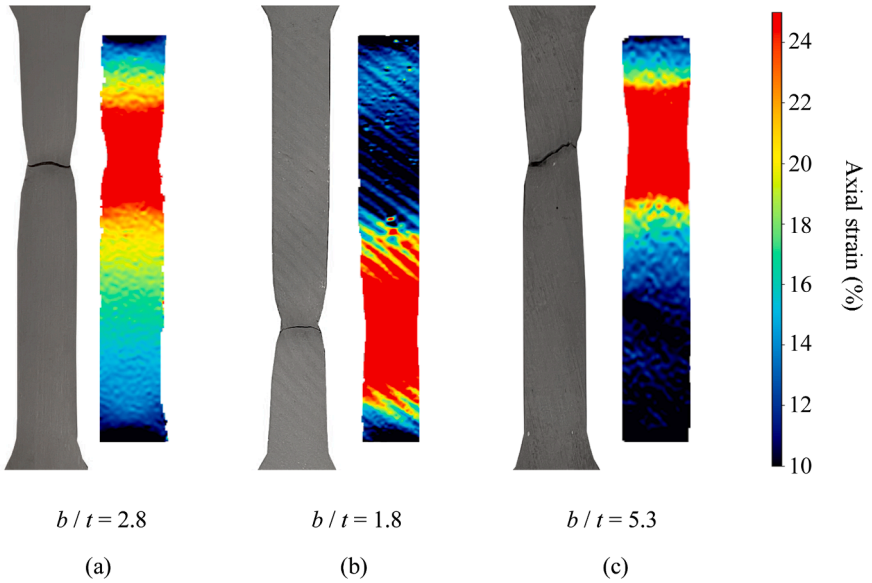


Fig. 21. Surface axial strains at fracture of typical machined for orientations: (a) $\theta = 0°$, (b) $\theta = 45°$ and (c) $\theta = 90°$.

5.3.5. *Influence of defects*

The impact of defects on the mechanical performance of WAAM materials is discussed herein based on the XCT scanning and tensile test results for the 8 mm and 12 mm-thick machined coupons. XCT scanning revealed that four coupons had somewhat higher porosity than others, namely P8-45-1-M, P8-45-2-M, P8-90-2-M, and A12-90-2-M. The mechanical performance of these coupons is therefore examined relative to the others. Fig. 28 compares the maximum porosity, as defined in Section 4.2, for all scanned coupons with their material properties (i.e., E, ν, f_y, f_u, ε_u and ε_f). The Young's modulus E, the Poisson's ratio ν and the yield strength f_y exhibited negligible influence from the porosity. The ultimate strength f_u of the most porous coupons, i.e. P8-45-1-M, P8-45-2-M, P8-90-2-M, is, on average, 15% lower than those without significant porosity, while no obvious decrease was observed for specimen A12-90-2-M since the porosity was less severe. Finally, the presence of pores strongly affects the ductility, as reflected by the reductions in ε_u and ε_f; the porous 8 mm-thick coupons, i.e. P8-45-1-M, P8-45-2-M, P8-90-2-M, exhibited a decrease up to 90% in ε_u and 93% decrease in ε_f. In contrast, the A12-90-2-M coupon showed a smaller reduction in ε_u and ε_f due to its lower porosity, as illustrated in Figs. 29(e) and 29(f). Such porosity has been shown to significantly reduce the ductility under monotonic tension, but have insignificant influence on the structural behaviour under monotonic compression [71]; fatigue life is also negatively affected by porosity [72].

5.3.6. *Comparison with as-welded properties from wire certificate*

In this section, the material properties obtained from the machined coupon tests in Table 8, excluding the impact of the surface undulations, are compared with the as-welded properties specified in the wire certificate in Table 1. Most examined WAAM materials failed to meet the minimum guaranteed yield strength f_y, except for those with nominal thicknesses of 3.5 mm and 5 mm. This can be attributed to the multiple thermal cycles and the slower cooling rate for WAAM compared with conventional welding. Most machined coupons reached the specified minimum ultimate strength f_u, except for some porous specimens. As shown in Table 8, the tested machined coupons generally displayed good ductility, with most of them meeting all the ductility criteria of Eurocode 3 for hot-rolled steels, i.e. $f_u/f_y > 1.05$ and $\varepsilon_f > 12\%$ for elastic global analysis, as specified in EN 1993-1-1 [73].

6. Microstructural analysis

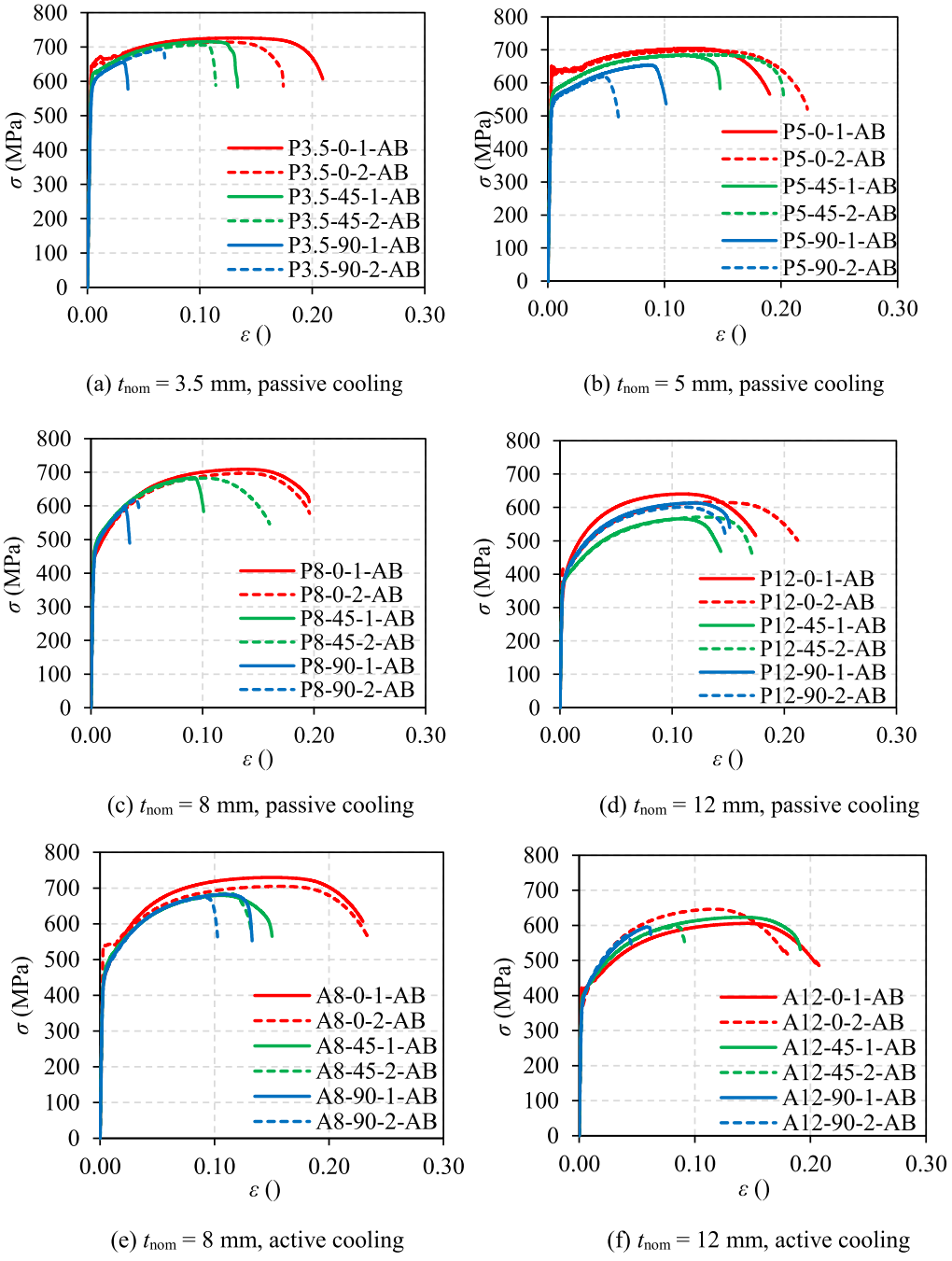
AM processes are characterised by the rapid solidification of metals and the intricate thermal histories, which significantly influence the underlying microstructure and the resulting mechanical properties of the materials [17,28,44]. To explore the mechanical properties from a metallurgical perspective, microstructural characterisation of the examined WAAM carbon steel was performed through Electron Backscatter Diffraction (EBSD) analysis. The sample preparations and findings from the EBSD analysis are described in this section.

6.1. *Preparation of metallographic samples*

Metallographic samples for microstructural analysis were extracted from the centre of the P3.5, P5, P8, P12, A8 and A12 WAAM plates, which were manufactured using different cooling methods and process parameters. For each plate, three samples were first mounted in bakelite, with their front, cross-section and side faces exposed, as shown in Fig. 30, and then prepared following the procedure recommended in ASTM E3-11 [74]. The preparation involved grinding using SiC papers progressively from 500 to 4000 grit size and then polishing using 6 μm, 3 μm and 1 μm diamond suspensions and finally a 0.04 μm OP-S solution, pH balanced using H_2O_2 and water in the ratios 7:3:10., resulting in a mirror-like surface before mounting onto stubs for EBSD analysis. The grain size and morphology and the texture were investigated using a Zeiss Sigma-500 scanning electron microscope (SEM) equipped with an Oxford Instruments Symmetry EBSD detector and forescatter electron (FSE) imaging. The metallographic samples for EBSD were tilted to 70° relative to the horizontal to generate diffraction patterns with sufficient intensity. A 60 μm aperture size, 15 mm working distance and 20 kV accelerating voltage were used to collect the data. Each sample surface was scanned at 1000× magnification to ensure sufficient grains across a wide region without losing sub-structure features. The EBSD patterns were acquired using Oxford Instruments Aztec software package [75] and post-processed analysed using MTEX [76].

6.2. *Microstructural characterisation*

The grain size distribution, phase proportion and texture of the examined WAAM material manufactured using different cooling



(a) t_{nom} = 3.5 mm, passive cooling

(b) t_{nom} = 5 mm, passive cooling

(c) t_{nom} = 8 mm, passive cooling

(d) t_{nom} = 12 mm, passive cooling

(e) t_{nom} = 8 mm, active cooling

(f) t_{nom} = 12 mm, active cooling

Fig. 22. Stress-strain curves of as-built coupons.

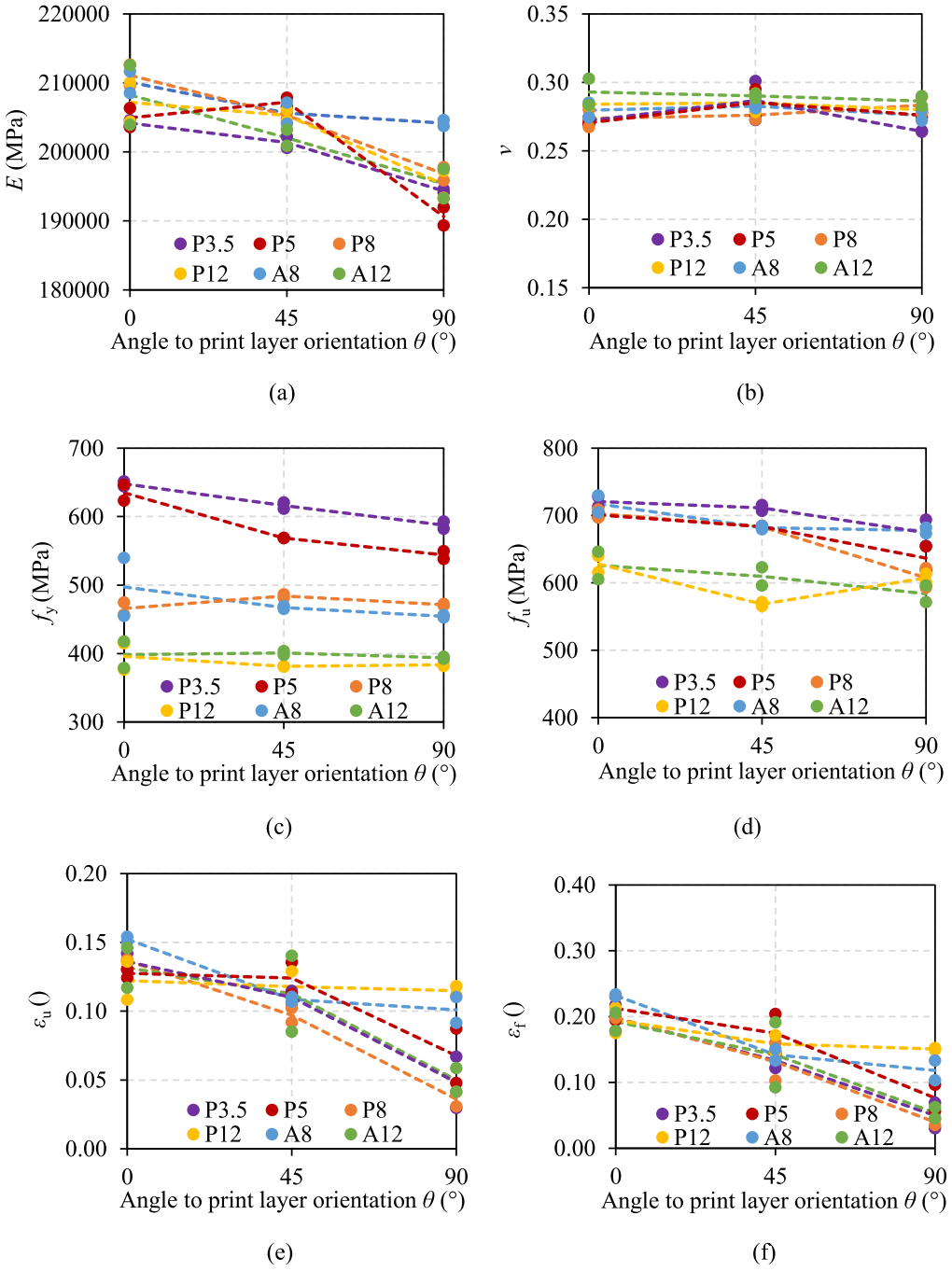


Fig. 23. (a) Young's Modulus E, (b) Poisson's ratio ν, (c) yield strength f_y, (d) ultimate strength f_u, (e) elongation at ultimate strength ε_u and (f) elongation at fracture ε_f at different angles θ of as-built tensile coupons.

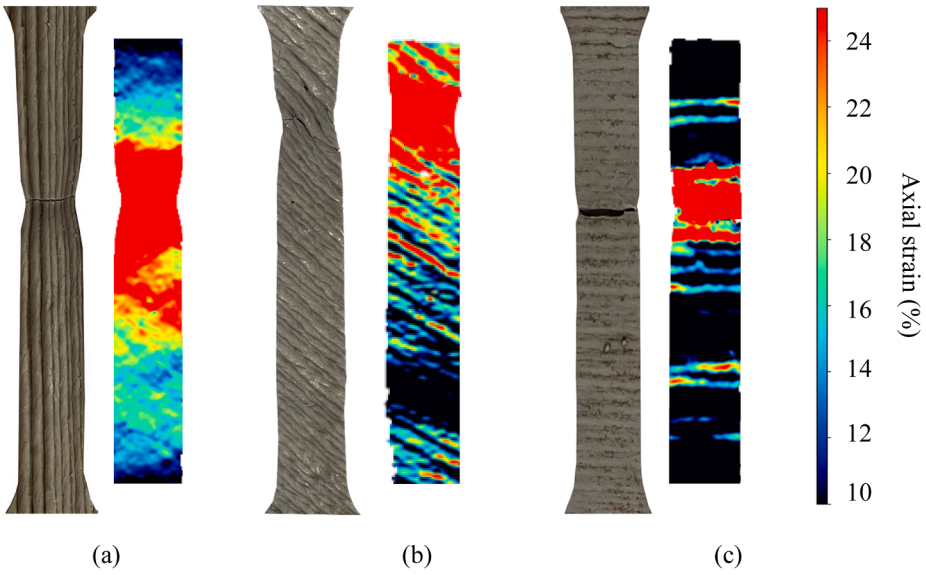


Fig. 24. Surface axial strains at fracture of typical as-built coupons for orientations: (a) $\theta = 0°$, (b) $\theta = 45°$ and (c) $\theta = 90°$.

methods and process parameters were characterised through EBSD analysis. Forescattered diffraction (FSD) imaging was used for EBSD mapping to provide information on surface topography and crystallographic orientation contrast. Figs. 31 and 32 show typical FSD images taken for samples from the P12 and A12 plates, coupled with the corresponding inverse pole figure (IPF) maps coloured with respect to the build direction, with overlaid grain boundaries, and {100}, {110} and {111} pole figures. The IPF maps show the orientation of individual grains relative to a specific sample direction – the build direction in this study, while the pole figures present the global texture, where each point represents the orientation of a specific crystallographic plane or direction relative to the sample reference frame. The contour level in pole figures, also referred to as the texture index, indicates the intensity of a preferred orientation compared to random orientations. It is noted that the texture was obtained from the crystallographic orientations of approximately 1000 grains within the scanned area. All the IPF and pole figures show no preferred crystallographic orientations in the examined material regardless of the cooling methods and process parameters, indicating nearly isotropic behaviour. This isotropy also explains the consistency of the Young's modulus E and yield strength f_y of the coupons loaded in the different directions relative to the deposition layers, and has also been reported by Weber et al. [44] and Huang et al. [17]. It is noted that some coupons had small differences in ultimate strength f_u in the different loading directions; this is attributed largely to the presence of porosity and lack-of fusion defects, rather than the crystallographic texture and grain shape. As expected, the body-centred cubic (BCC) ferritic phase was predominated in the material manufactured using the different cooling methods and process parameters, with only a

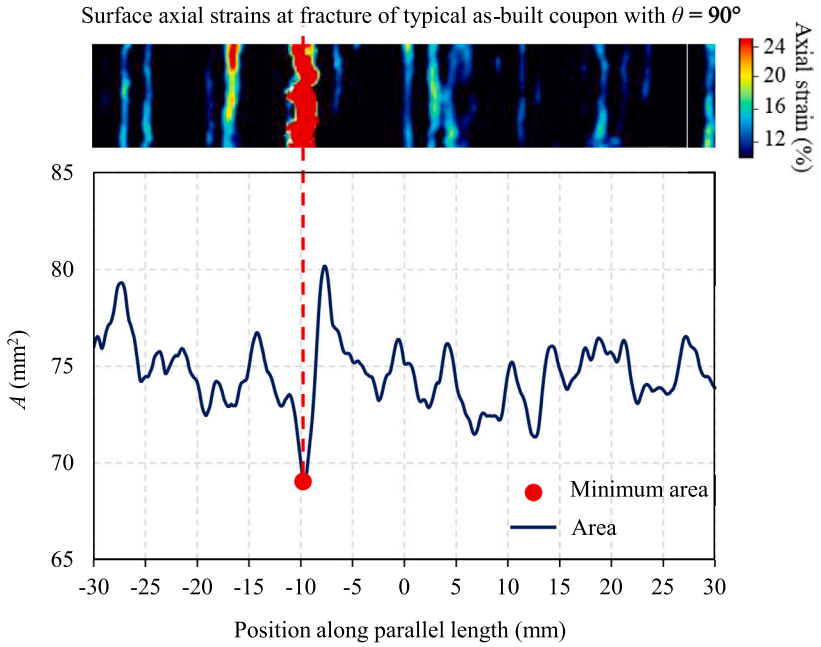


Fig. 25. Fracture position of an as-built coupon coinciding with the smallest cross-sectional area along its parallel length.

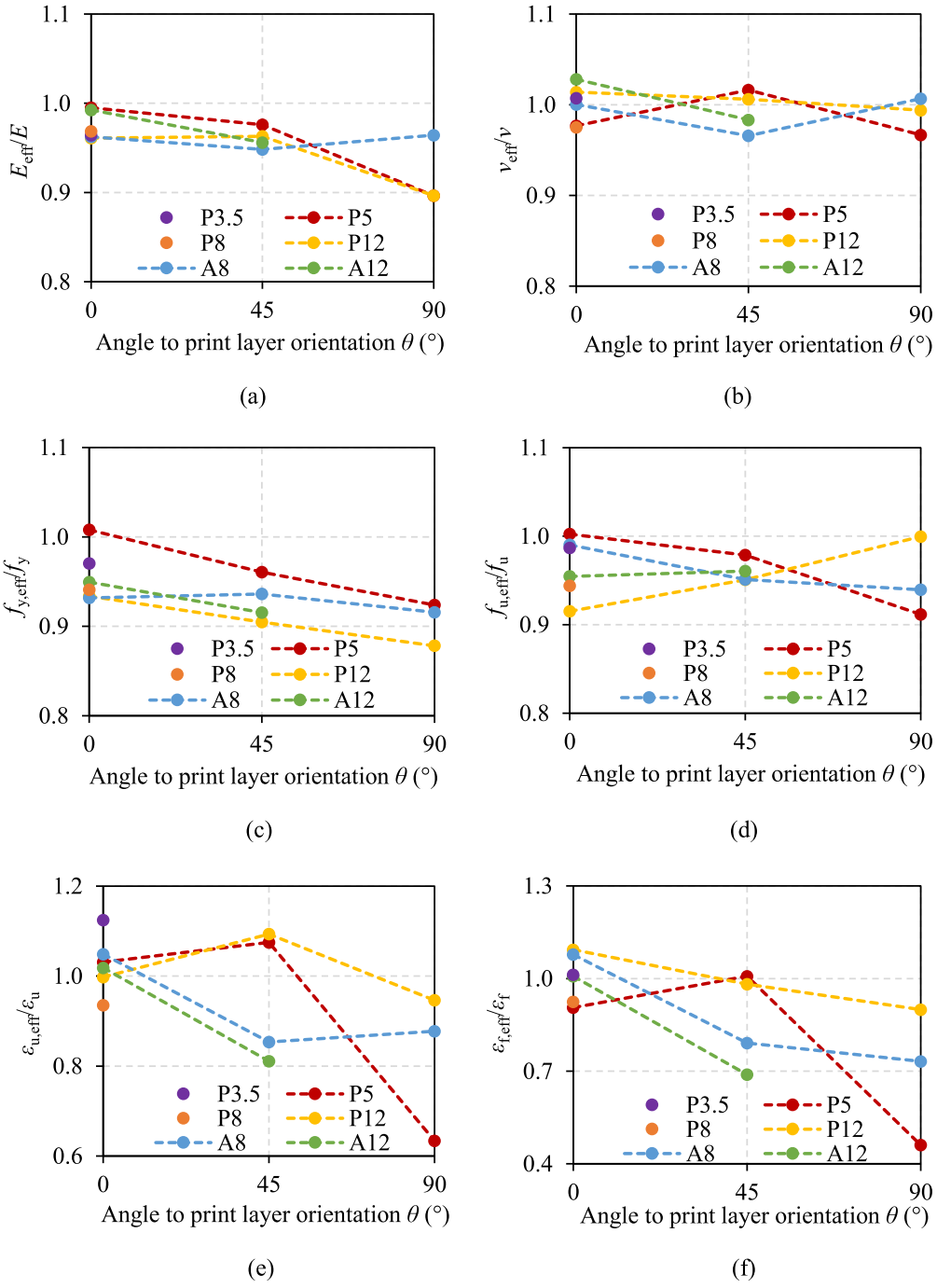


Fig. 26. Comparison of (a) Young's Modulus E, (b) Poisson's ratio ν, (c) yield strength f_y, (d) ultimate strength f_u, (e) elongation at ultimate strength ε_u and (f) elongation at fracture ε_f at different angles θ between as-built and machined coupons.

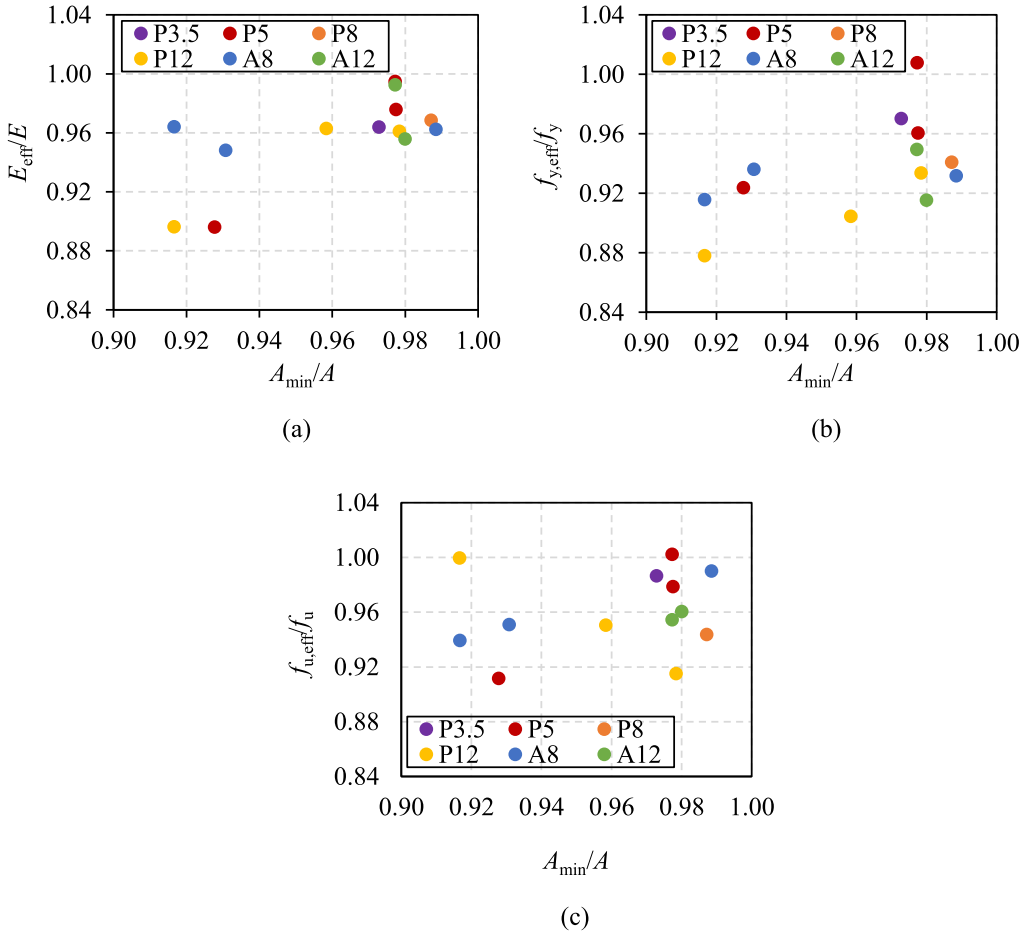


Fig. 27. Influence of A_{min}/A ratio on the (a) Young's Modulus E, (b) yield strength f_y and (c) ultimate strength f_u ratio between as-built and machined coupons.

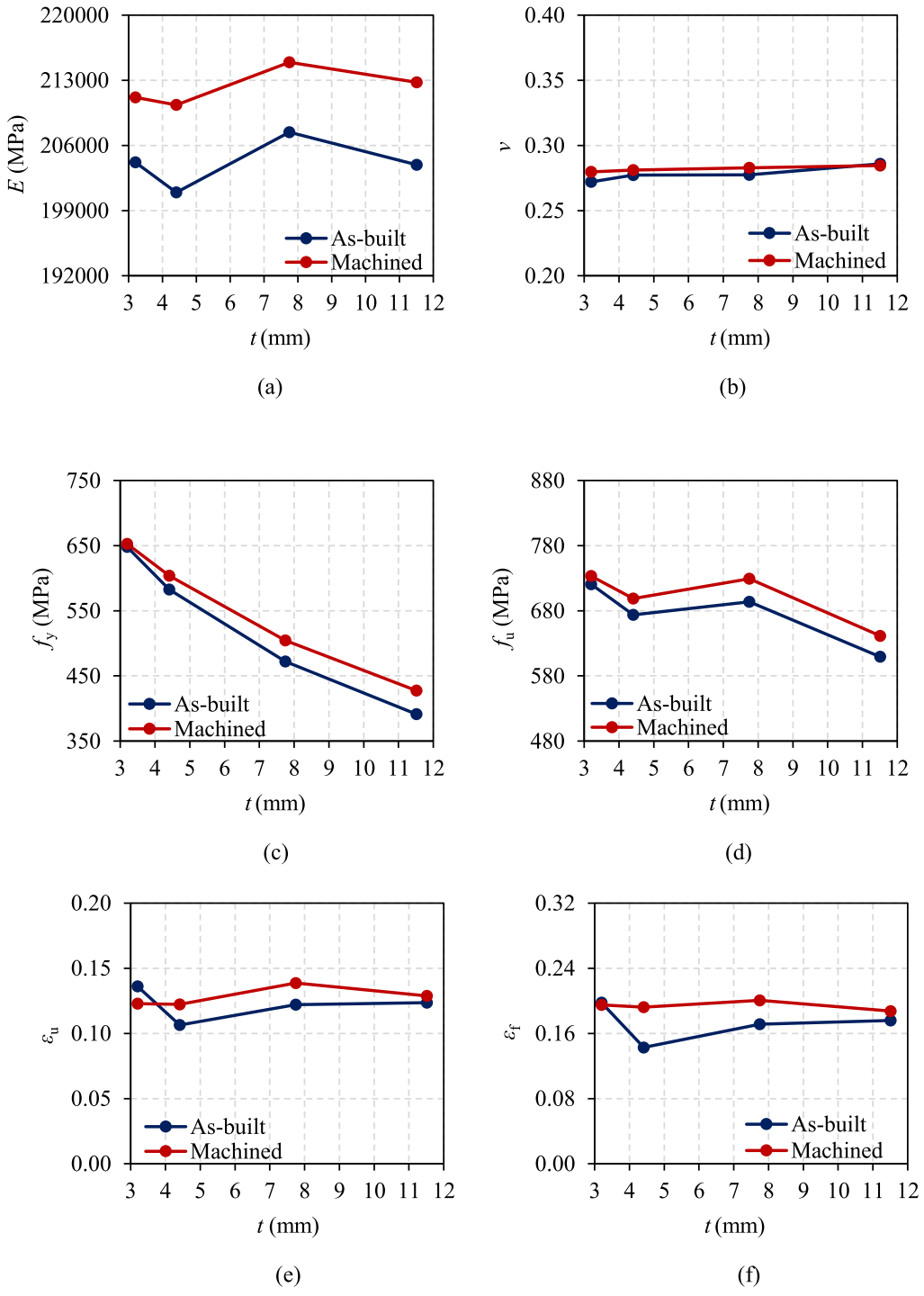


Fig. 28. Variation of averaged (a) Young's Modulus E, (b) Poisson's ratio ν, (c) yield strength f_y, (d) ultimate strength f_u, (e) elongation at ultimate strength ε_u and (f) elongation at fracture ε_f with average thickness.

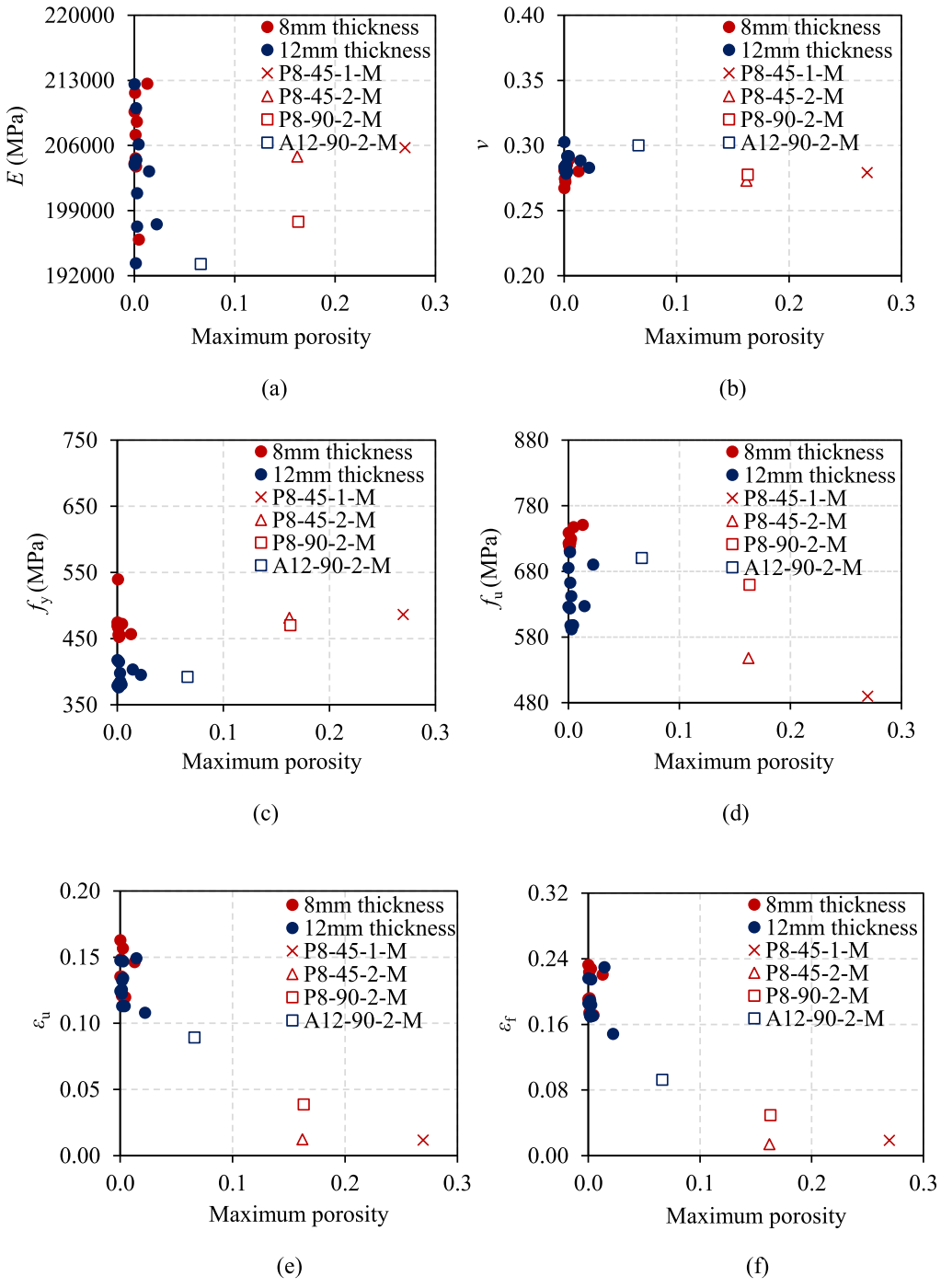


Fig. 29. Variation of (a) Young's Modulus E, (b) Poisson's ratio ν, (c) yield strength f_y, (d) ultimate strength f_u, (e) elongation at ultimate strength ε_u and (f) elongation at fracture ε_f with the maximum porosity.

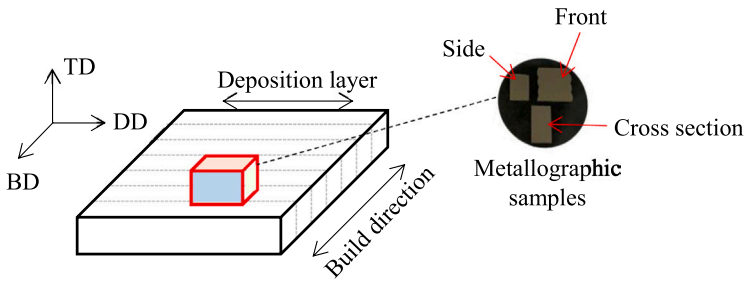


Fig. 30. Extraction of metallographic samples from WAAM plates.

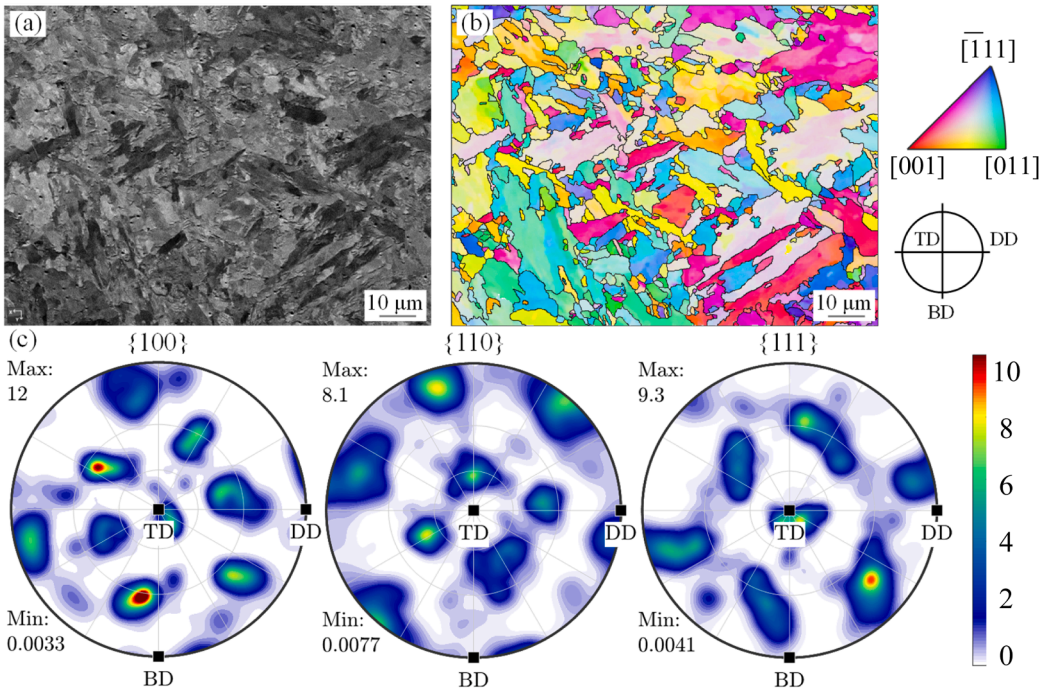


Fig. 31. Typical (a) FSD image, (b) inverse pole figure (IPF) map along the build direction and (c) pole figures of the ferrite phase of P12 sample.

small proportion of the austenitic face-centred cubic (FCC) phase.

It is well-established that the average grain size has a significant effect on the yield strength of the material, as described by the Hall-Petch relationship [77,78]. A smaller grain size means more grain boundaries, which can provide higher resistance to dislocation movement, thus leading to an increased yield strength of the material. In this study, the grain size d of each individual grain is defined as the diameter of an equivalent circle with the same area. The grain size distributions of all the examined WAAM material printed using the different cooling methods and process parameters are presented in Fig. 33, with their average grain size d_{avg} and average yield strength $f_{y,avg}$ of the machined coupons – excluding those with significant pores – and reported in Table 10. It can be seen that the material printed with the passive and active cooling methods had no difference in average grain size and yield

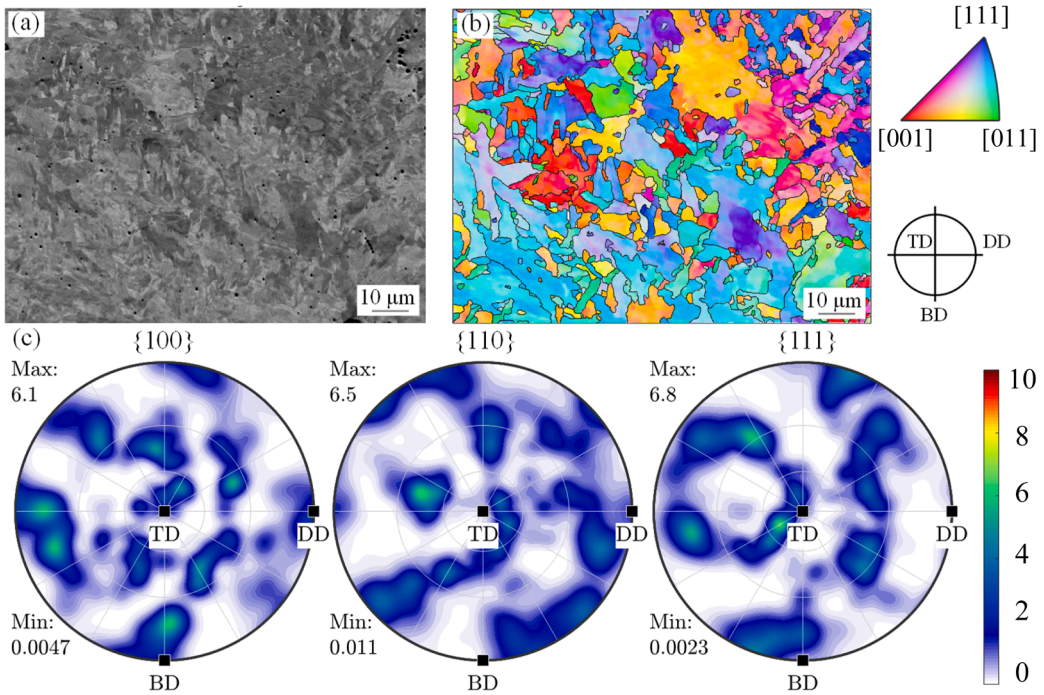


Fig. 32. Typical (a) FSD image, (b) inverse pole figure (IPF) map along the build direction and (c) pole figures of the ferrite phase of A12 sample.

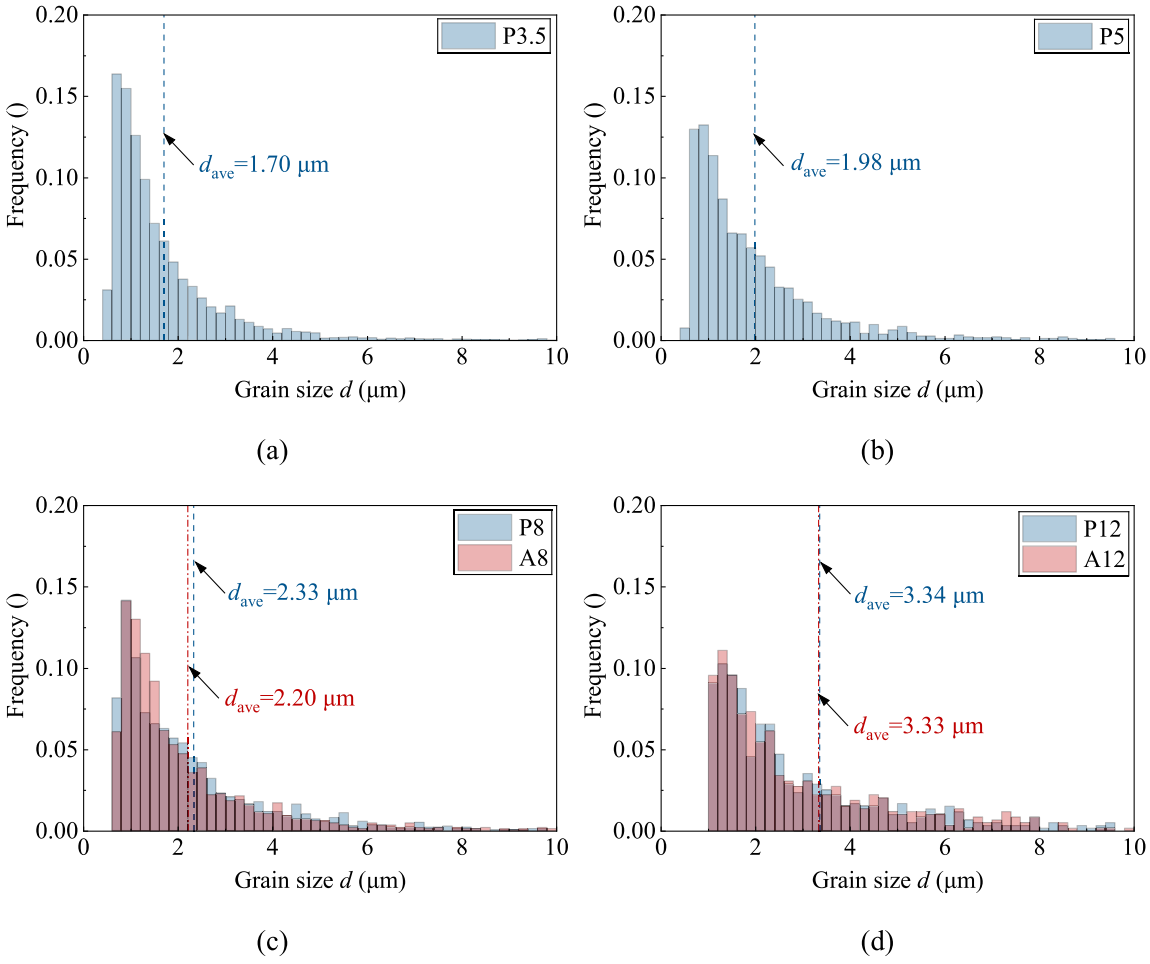


Fig. 33. Grain size distributions of (a) P3.5, (b) P5, (c), P8, A8 and (d) P12, A12 samples.

Table 10
Variation of the measured yield strength with the average grain size of examined WAAM steel.

Nominal thickness and cooling method of the material	$f_{y,avg}$ (MPa)	Average equivalent circular grain diameter (μm)
P3.5	653	1.70
P5	604	1.98
P8	494	2.33
P12	427	3.34
A8	510	2.20
A12	428	3.33

strength. Note that the cooling rates were not quantitively measured during the manufacture of the ovals; future work could be dedicated to the accurate measurement of local cooling rates from different cooling methods and the resulting effects on phase fractions and grain sizes. The coupons with the larger thicknesses had larger grain sizes, which explains their lower measured yield strengths; this finding is consistent with previous studies on WAAM carbon steel [17].

7. Conclusions

An experimental study has been conducted to examine the mechanical behaviour and microstructural properties of wire arc additively manufactured (WAAM) steel printed with different process parameters and cooling methods. The examined WAAM material featured ER90S-D2 welding wire, active and passive cooling and four different nominal wall thicknesses. A total of 72 tensile coupon tests were performed, with specimens extracted at three different angles relative to the print layer orientation, covering both as-built and machined surface finishes. 3D laser scanning was employed to capture the as-built surface geometries, X-ray computed tomography (XCT) scanning was conducted to examine the defects, and digital image correlation (DIC) was used to capture deformation and strain distributions during tensile testing.

From the surface geometry examinations, the surface roughness was found to increase with material thickness, while the cooling methods were shown to have an insignificant effect. The XCT results revealed high localised porosity in some coupon specimens, most likely due to external conditions / human errors; no significant influence from the different process parameters and cooling methods on the extent of defects was observed. The machined coupon test results indicated that all the examined WAAM steels generally exhibited nearly isotropic material behaviour in the elastic stage, which agrees with the homogeneous grain structure and weak crystallographic texture revealed in the electron backscattered diffraction (EBSD) analysis for all the samples. The undulating geometry of the as-built coupons, particularly for those oriented at 90° to the print layers, caused slight reductions in the Young's modulus and yield and ultimate strengths, and significant decreases in ductility due to localised strain concentrations. The applied active cooling method was shown to have minimal influence on the mechanical properties. On the contrary, the WAAM steels with different wall thicknesses, achieved through the use of different process parameters, thus resulting in different heat inputs and cooling rates, were shown to exhibit considerably different mechanical properties. The thicker samples displayed lower yield and ultimate strengths, which was attributed to the coarser grains caused by slower cooling, as observed in the

microstructural analysis. XCT effectively identified the internal pores in some machined coupon samples, which were shown to impact the mechanical properties, particularly the ductility, highlighting the need for defect monitoring and control in WAAM processes.

CRediT authorship contribution statement

Spinasa Athina: Writing – original draft, Visualization, Software, Methodology, Investigation, Formal analysis, Data curation. **Weber Ben:** Writing – review & editing, Software, Methodology, Investigation, Data curation, Conceptualization. **Meng Xin:** Writing – review & editing, Supervision, Methodology, Formal analysis, Conceptualization. **Zhang Ruizhi:** Writing – review & editing, Visualization, Software, Methodology, Investigation, Formal analysis, Data curation. **Nitawaki Masashi:** Software, Resources, Methodology, Investigation, Formal analysis, Data curation. **Gardner Leroy:** Writing – review & editing, Supervision, Resources, Project administration, Funding acquisition, Formal analysis, Conceptualization.

Declaration of Competing Interest

The authors declare that they have no known competing financial interests or personal relationships that could have appeared to influence the work reported in this paper.

Acknowledgements

This study was possible thanks to funding and support from the Shimizu Corporation, the Onassis Foundation and the National Research Fund of Luxembourg. The authors would also like to thank Paul Crudge and Alfredo Olivo for their assistance during the experiments.

Data Availability

Data will be made available on request.

References

[1] W. Gao, Y. Zhang, D. Ramanujan, K. Ramani, Y. Chen, C.B. Williams, C. Wang, Y. Shin, S. Zhang, P. Zavattieri, The status, challenges, and future of additive manufacturing in engineering, Comput. -Aided Des. 69 (2015) 68–89.
[2] A. Paolini, S. Kollmannsberger, E. Rank, Additive manufacturing in construction: a review on processes, applications, and digital planning methods, Addit. Manuf. 30 (2019) 100894.
[3] X. Guo, P. Kyvelou, J. Ye, L.H. Teh, L. Gardner, Experimental investigation of wire arc additively manufactured steel single-lap shear bolted connections, Thin-Walled Struct. 181 (2022) 110029.
[4] L. Gardner, Metal additive manufacturing in structural engineering – review, advances, opportunities and outlook, Structures 47 (2023) 2178–2193.
[5] ISO/ASTM 52900, Additive manufacturing - general principles - terminology, ASTM, 2017.
[6] S.W. Williams, F. Martina, A.C. Addison, J. Ding, G. Pardal, P. Colegrove, Wire and arc additive manufacturing, Mater. Sci. Technol. 32 (7) (2016) 641–647.
[7] J. Ye, P. Kyvelou, F. Gilardi, H. Lu, M. Gilbert, L. Gardner, An end-to-end framework for the additive manufacture of optimized tubular structures, IEEE Access 9 (2021) 165476–165489.
[8] I.H. Shah, N. Hadjipantelis, L. Walter, R.J. Myers, L. Gardner, Environmental life cycle assessment of wire arc additively manufactured steel structural components, J. Clean. Prod. 389 (2023) 136071.
[9] P. Kyvelou, C. Buchanan, L. Gardner, Numerical simulation and evaluation of the world's first metal additively manufactured bridge, J. Constr. Steel Res. 42 (2020) 405–416.
[10] T. Feucht, J. Lange, M. Erven, C.B. Costanzi, U. Knaack, B. Waldschmitt, Additive manufacturing by means of parametric robot programming, Constr. Robot. 4 (2020) 31–48.
[11] P. Kyvelou, A. Spinasa, L. Gardner, Testing and analysis of optimized wire arc additively manufactured steel trusses, J. Struct. Eng. 150 (3) (2024) 04024008.
[12] X. Meng, L. Gardner, Hybrid construction featuring wire arc additive manufacturing: review, concepts, challenges and opportunities, Eng. Struct. 326 (2025) 119337.
[13] Liu S. Structural design of the first 3D metal printing structure in Hong Kong using WAAM: innovation, challenges and insights. The 1st International Conference on Engineering Structures. Guangzhou, China; 2024.
[14] H. Seifi, A. Rezaee Javan, S. Xu, Y. Zhao, Y.M. Xie, Design optimization and additive manufacturing of nodes in gridshell structures, Eng. Struct. 160 (2018) 161–170.
[15] J. Reimann, P. Henckell, Y. Ali, S. Hammer, A. Rauch, J. Hildebrand, J. P. Bergmann, Production of topology-optimised structural nodes using arc-based additive manufacturing with GMAW welding process, J. Civ. Eng. Constr. 10 (2) (2021) 101–107.
[16] S.I. Evans, J. Wang, J. Qin, Y. He, P. Shepherd, J. Ding, A review of WAAM for steel construction – Manufacturing, material and geometric properties, design, and future directions, Structures 44 (2022) 1506–1522.
[17] C. Huang, P. Kyvelou, R. Zhang, B.T. Britton, L. Gardner, Mechanical testing and microstructural analysis of wire arc additively manufactured steels, Mater. Des. 216 (2022) 110544.
[18] V.A. Silvestru, I. Ariza, J. Vienne, L. Michel, A.M. Aguilar Sanchez, U. Angst, R. Rust, F. Gramazio, M. Kohler, A. Taras, Performance under tensile loading of point-by-point wire and arc additively manufactured steel bars for structural components, Mater. Des. 205 (2021) 109740.
[19] C.V. Haden, G. Zeng, F.M. Carter, C. Ruhl, B.A. Krick, D.G. Harlow, Wire and arc additive manufactured steel: Tensile and wear properties, Addit. Manuf. 16 (2017) 115–123.
[20] H. Xin, I. Tarus, L. Cheng, M. Veljkovic, N. Persem, L. Lorich, Experiments and numerical simulation of wire and arc additive manufactured steel materials, Structures 34 (2021) 1393–1402.
[21] T. Tankova, D. Andrade, R. Branco, C. Zhu, D. Rodrigues, L. Simões Da Silva, Characterization of robotized CMT-WAAM carbon steel, J. Constr. Steel Res. 199 (2022) 107624.
[22] V. Laghi, L. Arrè, L. Tonelli, G. Di Egidio, L. Ceschini, I. Monzón, A. Laguía, J. A. Dieste, M. Palermo, Mechanical and microstructural features of wire-and-arc additively manufactured carbon steel thick plates, Int. J. Adv. Manuf. Technol. 127 (2023) 1391–1405.
[23] Y. Khandelwal, R.K. Gupta, K.K. Verma, A. Mandal, A Study of microstructure and mechanical properties of wire arc additive manufactured component with ER70S6 alloy wire using CMT process, Gener. Mater. Process. Technol. 9 (2021) 133–146.
[24] C. Huang, P. Kyvelou, L. Gardner, Stress-strain curves for wire arc additively manufactured steels, Eng. Struct. 279 (2023) 115628.
[25] V. Laghi, M. Palermo, L. Tonelli, G. Gasparini, L. Ceschini, T. Trombetti, Tensile properties and microstructural features of 304L austenitic stainless steel produced by wire-and-arc additive manufacturing, Int. J. Adv. Manuf. Technol. 106 (2020) 3693–3705.
[26] V. Laghi, M. Palermo, G. Gasparini, V.A. Girelli, T. Trombetti, Experimental results for structural design of wire-and-arc additive manufactured stainless steel members, J. Constr. Steel Res. 167 (2020) 105858.
[27] V. Laghi, M. Palermo, G. Gasparini, V.A. Girelli, T. Trombetti, On the influence of the geometrical irregularities in the mechanical response of wire-and-arc additively manufactured planar elements, J. Constr. Steel Res. 178 (2021) 106490.
[28] P. Kyvelou, H. Slack, D. Daskalaki Mountanou, M.A. Wadee, T.B. Britton, C. Buchanan, L. Gardner, Mechanical and microstructural testing of wire and arc additively manufactured sheet material, Mater. Des. 192 (2020) 108675.
[29] J.P. Pragana, I.M. Bragança, L. Reis, C.M. Silva, P.A. Martins, Formability of wire-arc deposited AISI 316L sheets for hybrid additive manufacturing applications, J. Mater.: Des. Appl. 235 (12) (2021) 2839–2850.
[30] N. Hadjipantelis, B. Weber, C. Buchanan, L. Gardner, Description of anisotropic material response of wire and arc additively manufactured thin-walled stainless steel elements, Thin-Walled Struct. 171 (2022) 108634.
[31] J.V. Gordon, C.V. Haden, H.F. Nied, R.P. Vinci, D.G. Harlow, Fatigue crack growth anisotropy, texture and residual stress in austenitic steel made by wire and arc additive manufacturing, Mater. Sci. Eng.: A 724 (2018) 431–438.
[32] Z. Lin, K. Song, X. Yu, A review on wire and arc additive manufacturing of titanium alloy, J. Manuf. Process. 70 (2021) 24–45.
[33] F. Wang, S. Williams, P. Colegrove, A.A. Antonysamy, Microstructure and mechanical properties of wire and arc additive manufactured Ti-6Al-4V, Metall. Mater. Trans. 44 (2) (2013) 968–977.
[34] T. Klein, A. Arnoldt, R. Lahnsteiner, M. Schnall, Microstructure and mechanical properties of a structurally refined Al–Mg–Si alloy for wire-arc additive manufacturing, Mater. Sci. Eng.: A 830 (2022) 142318.
[35] K.S. Derekar, A review of wire arc additive manufacturing and advances in wire arc additive manufacturing of aluminium, Mater. Sci. Technol. 34 (8) (2018) 895–916.
[36] L. Tonelli, V. Laghi, M. Palermo, T. Trombetti, L. Ceschini, AA5083 (Al–Mg) plates produced by wire-and-arc additive manufacturing: effect of specimen orientation on microstructure and tensile properties, Prog. Addit. Manuf. 6 (3) (2021) 479–494.
[37] W.C. Ke, J.P. Oliveira, B.Q. Cong, S.S. Ao, Z.W. Qi, B. Peng, Z. Zeng, Multi-layer deposition mechanism in ultra high-frequency pulsed wire arc additive manufacturing (WAAM) of NiTi shape memory alloys, Addit. Manuf. 50 (2022) 102513.
[38] P. Dirisu, S. Ganguly, A. Mehmanparast, F. Martina, S. Williams, Analysis of fracture toughness properties of wire + arc additive manufactured high strength low alloy structural steel components, Mater. Sci. Eng.: A 765 (2019) 138285.
[39] A. Ermakova, A. Mehmanparast, S. Ganguly, J. Razavi, F. Berto, Investigation of mechanical and fracture properties of wire and arc additively manufactured low carbon steel components, Theor. Appl. Fract. Mech. 109 (2020) 102685.
[40] H. Ban, G. Shi, A review of research on high-strength steel structures, Proc. Inst. Civ. Eng. - Struct. Build. 171 (8) (2018) 625–641.
[41] J.H. Schmitt, T. Iung, New developments of advanced high-strength steels for automotive applications, Comptes Rendus Phys. 19 (8) (2018) 641–656.

[42] W.M. Garrison, Ultrahigh-strength steels for aerospace applications, J. Miner. 42 (5) (1990) 20–24.
[43] X. Meng, L. Gardner, Cross-sectional behaviour of cold-formed high strength steel circular hollow sections, Thin-Walled Struct. 156 (2020) 106822.
[44] B. Weber, X. Meng, R. Zhang, M. Nitawaki, T. Sagawa, L. Gardner, Tensile behaviour of WAAM high strength steel material and members, Mater. Des. 237 (2024) 112517.
[45] M.T. Chen, T. Zhang, Z. Gong, W. Zuo, Z. Wang, L. Zong, O. Zhao, L. Hu, Mechanical properties and microstructure characteristics of wire arc additively manufactured high-strength steels, Eng. Struct. 300 (2024) 117092.
[46] Z. Lin, C. Goulas, W. Ya, M.J.M. Hermans, Microstructure and Mechanical properties of medium carbon steel deposits obtained via wire and arc additive manufacturing using metal-cored Wire, Metals 9 (6) (2019) 673.
[47] L. Sun, F. Jiang, R. Huang, D. Yuan, C. Guo, J. Wang, Microstructure and mechanical properties of low-carbon high-strength steel fabricated by wire and arc additive manufacturing, Metals 10 (2) (2020) 216.
[48] T.A. Rodrigues, V. Duarte, J.A. Avila, T.G. Santos, R.M. Miranda, J.P. Oliveira, Wire and arc additive manufacturing of HSLA steel: Effect of thermal cycles on microstructure and mechanical properties, Addit. Manuf. 27 (2019) 440–450.
[49] U. Reisgen, R. Sharma, S. Mann, L. Oster, Increasing the manufacturing efficiency of WAAM by advanced cooling strategies, Weld. World 64 (8) (2020) 1409–1416.
[50] E. Aldalur, F. Veiga, A. Suárez, J. Bilbao, A. Lamikiz, Analysis of the wall geometry with different strategies for high deposition wire arc additive manufacturing of mild steel, Metals 10 (7) (2020) 892.
[51] T.A. Rodrigues, V. Duarte, R.M. Miranda, T.G. Santos, J.P. Oliveira, Current status and perspectives on wire and arc additive manufacturing (WAAM), Materials 12 (7) (2019) 1121.
[52] L. Gardner, X. Yun, A. Fieber, L. Macorini, Steel design by advanced analysis: material modeling and strain limits, Engineering 5 (2) (2019) 243–249.
[53] M. Kucukler, L. Gardner, L. Macorini, Lateral-torsional buckling assessment of steel beams through a stiffness reduction method, J. Constr. Steel Res. 109 (2015) 87–100.
[54] AWS A5.28/A5.28M:2005, Specification for low-alloy steel electrodes and rods for gas shielded arc welding, American Welding Society, 2005.
[55] AWS D1.1/D1.1M-2010, Structural Welding Code—Steel, American Welding Society, 2010.
[56] EN1011-2:2001, Welding Recommendations for welding of metallic materials Part 2: Arc welding of ferritic steels, European committee for standardization, 2020.
[57] Z. Al-Nabulsi, J.T. Mottram, M. Gillie, N. Kourra, M.A. Williams, Mechanical and X ray computed tomography characterisation of a WAAM 3D printed steel plate for structural engineering applications, Constr. Build. Mater. 274 (2021) 121700.
[58] Oqton, Inc, Geomagic Wrap 2017, ⟨https://www.oqton.com/geomagic-wrap⟩, Version 2017.0.2:64.
[59] Robert McNeel & Associates, Rhino 6, ⟨https://www.rhino3d.com/⟩, Version 6.
[60] EN ISO 25178-2:2022. Geometrical product specifications (GPS) – Surface texture: Areal -Part2: Terms, definitions and surface texture parameters. European Committee for Standardization; 2022.
[61] ASME B46.1-2009, Surface texture (surface roughness, waviness and lay), American Society of Mechanical Engineers, 2010.
[62] J. Xiong, Y. Li, R. Li, Z. Yin, Influences of process parameters on surface roughness of multi-layer single-pass thin-walled parts in GMAW-based additive manufacturing, J. Mater. Process. Technol. 252 (2018) 128–136.
[63] A. Lopez, R. Bacelar, I. Pires, T.G. Santos, J.P. Sousa, L. Quintino, Non-destructive testing application of radiography and ultrasound for wire and arc additive manufacturing, Addit. Manuf. 21 (2018) 298–306.
[64] Volume Graphics, myVGL 2023, ⟨https://www.volumegraphics.com/myvgl⟩, Version 2023.3 64-bit.
[65] EN ISO 6892-1:2019, Metallic materials -Tensile testing - Part1: Method of test at room temperature, European Committee for Standardization, 2019.
[66] LaVision GmbH, DaVis 10, ⟨https://www.lavision.de/en/products/davis-software/⟩, Version 10.2.1.
[67] W. Ramberg, W.R. Osgood, Description of stress-strain curves by three parameters. National advisory committee for aeronautics, Tech. Note 902 (1943).
[68] E. Mirambell, E. Real, On the calculation of deflections in structural stainless steel beams: an experimental and numerical investigation, J. Constr. Steel Res. (2000) 109–133.
[69] M. Kucukler, Z. Xing, L. Gardner, Behaviour and design of stainless steel I-section columns in fire, J. Constr. Steel Res. 165 (2020) 105890.
[70] Y. Bao, T. Wierzbicki, On fracture locus in the equivalent strain and stress triaxiality space, Int. J. Mech. Sci. 46 (1) (2004) 81–98.
[71] X. Meng, B. Weber, M. Nitawaki, L. Gardner, Optimisation and testing of wire arc additively manufactured steel stub columns, Thin-Walled Struct. 189 (2023) 110857.
[72] E. Akgun, X. Zhang, R. Biswal, Y. Zhang, M. Doré, Fatigue of wire+arc additive manufactured Ti-6Al-4V in presence of process-induced porosity defects, Int. J. Fatigue 150 (2021) 106315.
[73] EN 1993-1-1:2022, Eurocode 3 - Design of steel structures - Part1-1: General rules and rules for buildings, European Committee for Standardization, 2022.
[74] ASTM E3-11:2017, Standard Guide for Preparation of Metallographic Specimens, ASTM, 2017.
[75] AZtec, Oxford Instruments, ⟨https://nano.oxinst.com/products/aztec⟩.
[76] F. Bachmann, R. Hielscher, H. Schaeben, Texture analysis with MTEX – free and open-source software toolbox, Solid State Phenom. 160 (2010) 63–68.
[77] E.O. Hall, The Deformation and ageing of mild steel: III Discussion of results, Proc. Phys. Soc., Sect. B 64 (9) (1951) 747–753.
[78] N. Petch, The cleavage strength of polycrystals, J. Iron Steel Inst. 174 (1953) 25–28.